Monitoring Global Fires from EOS-MODIS

The MODIS Fire Science Team:
Yoram J. Kaufman l, Chris Justice2, Luke Flynn 3, Jackie Kendall 4, Elaine Prins 5, Darold E. Ward 6, P. Menzel 7 and A. Setzer 8

(1) NASA/Goddard SFC, Laboratory for Atmospheres (913), Greenbelt MD 20771

(2) Dept. Geog, U. of Maryland and NASA/Goddard SFC (923), Greenbelt MD 20771,

(3) Hawaii Inst. of Geoph. and Planet., U. of Hawaii, 2525 Correa Rd, Honolulu, HA 96822

(4) Science Systems and Applications Inc, 5900 Princess Garden Parkway, Lanham, Md 20706

(5) U. of Wisconsin, Madison Corp. Inst. for Metor. Satellite Studies, 1225 West Dayton st., Madison, WI 53706

(6) Intermountain Research Station, Forest Service, USDA, Missoula, MT 59807

(7) NOAA/NESDIS, 1225 West Dayton st., Madison, WI 53706

(8) INPE C. Postal 515, 12201- S.J. Campos - SP - Brazil

Abstract

NASA plans to launch the Moderate Resolution Imaging Spectroradiometer (MODIS) on the polar orbiting Earth Observation System (EOS) for morning and evening global observations in 1998 and afternoon and night observations in 2000. These 4 MODIS daily fire observations will advance global fire monitoring with special 1 km resolution fire channels at 4 μm and 11 μm, with high saturation at 500K and 400K respectively. MODIS data will also be used to monitor burn scars, vegetation type and condition, smoke aerosols, water vapor and clouds for overall monitoring of the fire process and its effects on ecosystems, the atmosphere and climate.

The MODIS fire science team is preparing a series of algorithms for routine monitoring of fires and their properties. These algorithms are being designed to allow fire identification and characterization as well as mapping of burn scars. Using the elevation above background of the thermal signature, fires are separated from the background signal and evaluated. A data base of the daily fire occurrence and location, the apparent thermal energy emitted from the fire and a rough estimate of the smoldering/flaming ratio is generated from the thermal signature and archived. This information is expected to be used in monitoring the spatial and temporal distribution of fires in different ecosystems, in detecting changes in the fire distribution, new fire frontiers, wild fires, and changes in the density of the fires or their relative strength. This information will be used for the subsequent estimation of the emissions of trace gases and particulates from the fires.

The MODIS active fire product will be generated at a lkm resolution and summarized on a grid of 10 km and 0.5° resolution. Fire information will be presented as a daily product and summarized as eight day and monthly products. Amongst other product enhancement activities in the post-launch period, we plan to combine the MODIS 2 or 4 daily fire products with a detailed diurnal cycle of the fires from geostationary satellites.

Global lkm AVHRR data are currently being used to prototype aspects of the MODIS global fire products. Sensitivity studies, and analyses of aircraft and satellite data from the Yellowstone wild fire of 1988 and prescribed fires in the Smoke Cloud and Radiation (SCAR) field experiments are being used to evaluate and validate the fire algorithms and to establish the relationship between the fire apparent properties and the emission of aerosol and trace gases from the fire.

1. INTRODUCTION

Biomass burning is a major source of trace gases and aerosol particles, with significant ramifications for atmospheric chemistry, cloud properties and radiation budget (Crutzen et al., 1979; Crutzen and Andreae, 1990, Kaufman et al., 1992; Kaufman and Nakajima, 1993) and consequently to climate (Dickinson, 1993; Andreae, 1995; IPCC, 1995; Penner et al., 1992). Biomass burning contributes about a quarter of the global emission of greenhouse gases. Even though this is less than the contribution of industrial/urban pollution, the uncertainty in the emissions from biomass burning are larger than that of industrial emission (Intergovernmental Panel on Climate Change - IPCC, 1995). The rate of production of biomass burning aerosols is not much smaller than the production of sulfate particles from industrial/urban sources (Radke et al., 1991; Penner et al., 1992; IPCC, 1995). These particles were shown to be effective cloud condensation nuclei (Warner and Twomey, 1967; Hobbs and Radke, 1969), affect cloud drop size and reflectivity (Kaufman and Nakajima, 1993; Kaufman and Fraser, 1996) and may have a similar radiative forcing to that of sulfates (Penner et al., 1992). The combined effect of biomass burning aerosols and aerosols originating from industrial/urban activities, is considered the largest identified uncertainty in assessing a possible anthropogenic climate change (Hansen and Lacis, 1990).

Fire is also a significant and continuous factor in the ecology of savannas, boreal forests and tundra, and plays a major role in deforestation in tropical and sub-tropical regions. On a periodic basis, extensive fires also occur in many temperate biomes such as forests, grasslands, and chaparral. Fire is an integral part of land use in many parts of the World, particularly in the tropics. Since the discovery of the importance of biomass burning in the tropics (Crutzen et al., 1979) over 2 decades ago, large effort has been exerted to address this atmospheric process (see review by Crutzen and Andreae, 1990). However we do not have an accurate assessment of the global sources and emissions from biomass burning. The traditional approach and that adopted as the IPCC methodology for national emission estimates, is based on the FAO (Food and Agricultural Organization) statistics of population and agricultural practices (Hao, 1994, Skole et al. 1994). Other assessments use operational remote sensing of fires (Setzer and Pereira, 1991) from the polar orbiting NOAA (National Oceanic and Atmospheric Administration) AVHRR sensor. Simultaneous remote sensing of smoke and fires were suggested by Kaufman et al.

(1990a and b; 1994). New approaches, incorporating remote sensing of burn scars left by fires are also emerging (Justice et al, 1996).

In this paper we shall review the heritage of remote sensing of fires from satellites and its applications, the limitations in the present satellite capability and the strategy in the design of the MODIS sensor and MODIS fire detection algorithm to improve it.

2. THE HERITAGE FOR FIRE REMOTE SENSING

Regional remote sensing of fires was achieved using the VAS sensors on the GOES geostationary platforms and the polar orbiting NOAA AVHRR sensors. VAS can be used to locate active fires by utilizing the visible, 4 μm and 11 μm data. Since 1980 the VAS instruments on GOES 4-7 have provided multispectral monitoring of the Western Hemisphere. The GOES, positioned at a height of 36,000 km at a fixed point above the Equator, has the advantage of sensing the earth and fires diurnally. GOES VAS was scheduled to sample fires at most every 3 hours with a spatial resolution at 4 μm and 11 μm of 7 and 14 km, respectively. GOES-8, launched in 1994, increased the temporal (every 15 minutes in North America, half-hourly elsewhere) and spatial resolution (4 km in the IR bands), thus enabling improved detection of fire characteristics and aerosol loading and transport (Menzel and Prins, 1996; Prins and Menzel, 1996a). Prins and Menzel (1992; 1994) developed an automated algorithm to detect fires and determine the sub-pixel size of the active fire(s) and average fire temperature based on an adaptation of the Dozier algorithm (1981).

The GOES Automated Biomass Burning Algorithm (ABBA) is a dynamic multispectral thresholding algorithm which utilizes regional thresholds derived from the satellite data (visible, 4 μm, and 11 μm) for fire pixel identification and incorporates ancillary data to correct for water vapor attenuation, surface emissivity, and solar reflectivity. Figure 1 shows examples of GOES-8 fire detection in the Northwest US. GOES-8 observations of individual fires during the Smoke Cloud and Radiation (SCAR-C) field experiment based in California were verified using aircraft and field observations (Menzel and Prins, 1996). Several prescribed burns (Figure la) were initiated on 21 September 1994 in Washington in association with the SCAR-C experiment including the Quinault fire (48 acres), the Simpson fire (95 acres), and the ITT fire (97 acres). The fires outlined in Figure lb represent wildfires

in Northern California which were evident in the GOES-8 imagery over several days during SCAR-C. Figure 2 provides an example of initial GOES-8 ABBA diurnal fire monitoring results for 24 August 1995, one of the peak burning days during the Smoke Cloud and Radiation (SCAR-B) field experiment in Brazil. Throughout SCAR-B the number of fire pixels detected in South America with the GOES-8 ABBA at 1745 UTC ranged from 100 to over 3500; this was on average 2 to 4 times greater than that observed 3 hours earlier or later and 20 times greater than that observed at 1145 UTC (Prins and Menzel, 1996b).

The current sequence of NOAA Polar Orbiting Environmental Satellites (NPOES) has been in continuous operation since October 1978. They include the Advanced Very High Resolution Radiometer (AVHRR) which is a scanning radiometer measuring reflected and emitted radiation in two IR channels (3.75 μm and 11 μm). On-board calibration uses measurements of deep space and a black-body of known temperature. Unfortunately, the channels, developed for observation of sea surface temperature, saturate at 325K. A non-linearity in their response and even a folding of the values around the saturation temperature was discovered (Setzer and Verstrate, 1994), limiting the success of applications of detection and inversion algorithms. The viewing geometry gives rise to a 1.1 km ground resolution for pixels at nadir, similar to the planned MODIS IR channels. The wide scan angle (55") leads to pixels at image edges being over three times the size of pixels at nadir, and overlapping each other. An example of NOAA AVHRR lkm fires and burn scars observed for the Okavango Delta of Botswana is provided in Figure 3.

Dozier (1981) introduced a theoretical approach to study sub-pixel temperature fields using the 3.7 and 11 μm channels. He approximated the temperature field of each pixel by two areas of uniform temperature: the background area, and a target area which occupies some fraction from 0 to 1 of the pixel. Using his model, Dozier was able to show that a sub-resolution high temperature target is detectable because it has a greater effect in the 3.7 μm channel than in the 11 μm channel. He also derived a pair of simultaneous equations that could be solved for the temperature and the size of the hot target given the background temperature and the brightness temperatures at 3.7 and 11 μm. These equations are restricted to pixels that are unsaturated in both channels. The fire has to be strong enough to have a significantly larger impact on the 11 μm channel than the background

variability. This limits the applicability of the approach and a different approach is used for MODIS. Background temperature is estimated from adjacent pixels. Dozier suggested using a split-window technique to calculate a correction factor for the effect of atmospheric water vapor on the inversion.

The first applications of fire detection with AVHRR were on fixed targets of known location. Matson and Dozier (1981) used NOAA-6 nighttime imagery to detect high temperature industrial sources in Detroit and waste gas flares in the Persian Gulf. Similarly, Muirhead and Cracknell (1984) detected gas flares associated with oil fields in the North Sea using daytime NOAA-6. Following these studies of fixed targets, the AVHRR was used to detect vegetation fires. Matson et al. (1984) used daytime NOAA-6 and 7 imagery over the U.S. and Brazil to detect fires based on enhanced temperatures in the 3.7 μm channel. They also reported on an experimental operational fire monitoring project in the western U.S that was based on manual inspection of the 3.7 μm and 11 μm images alternating on a screen. More importantly, these detections were largely verified by US Forest Service stations, timber companies and local police. Muirhead and Cracknell (1984) also looked at vegetation fires by applying their technique to the detection of straw burning in Great Britain using daytime NOAA-7 imagery.

Flannigan and Vonder Haar (1986) and Flannigan (1985) developed the first automated (i.e. non-interactive) set of fire detection criteria. They used both daytime and nighttime data from NOAA-7 to monitor a severe forest fire outbreak in north-central Alberta, Canada. They were able to compare and validate satellite detections with Alberta Forest Service daily reports of fire location and size, using late afternoon aerial reconnaissance. Of the 41% of fires that were visible to the satellite (unobstructed by clouds), 80% were detected by their detection criteria. Based on comparison with the reconnaissance information, the AVHRR-based fire size estimates were 70% too large for small fires and 50% too small for large fires. A number of case studies were then reported from diverse regions (Matson et al. 1987, Matson and Holben 1987, Stephens and Matson 1989, Langaas and Muirhead 1988). These studies included an increasingly sophisticated discussion of the limitations and problems associated with fire detection with the AVHRR. This included effects of fixed, non-fire sources (Stephens and Matson, 1989), detection of and obstruction due to smoke plumes (Matson et al. 1987, Matson and Holben 1987), and effects of surface emissivity, pixel overlap at non-nadir scan angles and incorporation of

recently burnt warm areas into the two-element temperature field of the Dozier model (Langaas and Muirhead, 1988).

Lee and Tag (1990) presented an alternative approach to non-interactive fire detection. They subjectively chose a threshold fire temperature and used the Dozier model to develop a look-up table specifying which combinations of satellite measurements constituted a positive fire detection. Atmospheric corrections were included in the estimation of background temperatures using the method of McClain et al. (1985). They applied their technique to nighttime imagery over the San Francisco area and the Persian Gulf.

The saturation of the 3.7 μm channel on AVHRR prohibits distinction between small and large fires and between smoldering and flaming fires. In order to use AVHRR fire detection in regional assessments of emissions from fires, Kaufman et al. (1990a, b) applied fire and smoke detection from NOAA-9 data. Fires were detected in pixels that met three detection criteria. The first criterion was for the 3.7 μm channel brightness temperature to be elevated above a set threshold indicating a fire is present. The second criterion specified that the difference between the 3.7 μm and 11 μm temperatures must be at least l0K, to avoid hot exposed soils, and the third criterion used the 11 μm temperature to eliminate false detections from cool clouds, with small drop size, that are highly reflective in the 3.7 μm band. In regions where the smoke was clearly identified to originate from specific groups of fires, the average emission of particulates per fire was calculated and used to convert the total seasonal number of fires into an emission estimate.

Justice et al. (1996) and Scholes et al. (1996) combined AVHRR fire information in a dynamic model to generate improved trace gas and particulate emission estimates for Southern Africa. The approach combined satellite data on fire distribution and timing with fuel load calculated by a simplified ecosystem production model and ground based measurements of emission ratios (Ward et al. 1996, Shea et al. 1996). Daily fires detected by the AVHRR for the entire burning season were calibrated to provide burned area estimates using Landsat MSS data. The algorithm used for fire detection is described by Kendall et al. (1996) and is the basis for the IGBP-DIS community consensus algorithm for the AVHRR. This trace gas modeling was part of a larger body of fire related research as part of the IGBP Southern African Fire Atmosphere Research Initiative (SAFARI) (Andreae et al.

1994, Thompson 1996). The fire data generated by from the AVHRR were used to better understand trace gas trajectories and atmospheric chemistry (Thompson et al 1996).

Setzer and Pereira (1991) started the first regional operational fire monitoring program in Brazil. Since 1989 they have monitored fire occurrence for each fire season. Using NOAA-11 data in 1989, 96% of detected fires were verified by ground crews and there were no reports of missing fires. Setzer and Pereira (1991) used a fixed 3.7 μm temperature threshold to flag potential fires but also required that a smoke plume be identified by manual inspection of imagery in the AVHRR 0.64 μm channel for there to be a positive detection. In order to get a regional estimate of burned area over a burning season, they used a comparison of NOAA-g/AVHRR and Landsat/TM to determine that the average fire size is 0.7 of an AVHRR pixel, and assumed that the average duration of a fire was 1.5 days. Pereira et al. (1991) used AVHRR data from 'five consecutive days and Landsat/TM data from the sixth day to evaluate the accuracy of fire detection and burned area estimates.. All AVHRR-detected fires had corresponding TM scars. They found that on average the fire size was 43% of the AVHRR pixel size. Pereira and Setzer (1993) detected deforestation fires using a fixed 3.7 μm threshold applied to raw digital counts instead of derived brightness temperatures.

Although AVHRR was never built for fire detection, and as indicated, suffers from several drawbacks in this regard, it provides the best experience accumulated so far in orbital detection of vegetation fires. With over ten years of assorted applications in fire studies, some of its results can be used to identify MODIS fire product needs and assist in their design. In particular, the multi-year products of fire regional and temporal distributions over Africa from the Joint Research Center, Italy and ESA-ESRIN, Italy and the operational real-time detection program of INPE, Brazil, are good indicators of the potential contribution from MODIS standard fire products.

For example, Figure 4 shows a sequence of maps with the number of AVHRR fire pixels detected over Brazil in each month of the unusually dry season of 1991, when excessive burning took place. The monthly total number of fire pixels for Brazil in 1991 are summarized in Table 1. The peak in fire activity usually occurs in the last two weeks of August and first week of September and almost all fires have

anthropogenic origin, lasting only a few hours. The last map shows the cumulative fire activity for the season, with about 470 thousand fire pixels; a high concentration of fires is seen along the southern boundary of the Amazon basin, where conversion of natural forests and savannas to agriculture and pasture land is taking place at intensive rates. A shift in the zones affected by fires towards the north is also clear on the monthly sequence, resulting from the climatological northward advance of the dry season.

Similar data exists also for different years, allowing a more extended analysis. Using the same kind of weekly data, the total number of fire pixels for the June-October period of 1992 to 1994 is summarized in Table 1. It shows large annual variations. In 1995 the data are shown only till Aug 17, due to a change of satellites on Aug 18 from the early afternoon pass of NOAA-14 to the early night images of NOAA-12, and a corresponding. strong reduction in the fire count. Most fires in Brazil start in the afternoon to obtain higher combustion efficiencies taking advantage of a dryer air. Such differences in imaging schedule have therefore an important role. MODIS AM1 with its morning and late night overpasses will certainly miss a large number of fires in tropical regions with biomass burning as in South America and Africa. An improved fire detection by MODIS will be achieved after the launch of the PM platform in 2000.

The above cumulative fire data is produced on a weekly basis for a grid with cells of 0.5 degree of latitude and longitude, and is updated daily, after the satellite early afternoon pass. It is available through the Internet at the site http://www.nma.embrapa.br/projetos/qme/queimadas.html. It is distributed to newspapers that regularly publish the maps, and to atmospheric modelers studying emissions and transport of gases and aerosols. Other INPE operational fire products include daily maps of the AVHRR fire pixel detection over Brazil and some neighboring countries; these are found at http://condor.dsa.inpe.br/ult-focos. A summary of main advantages and limitations of the AVHRR technique used is found in Setzer (1994) and Setzer and Malingreau (1996).

Cahoon et al. (1991) examined a large fire in China using NOAA-9 data, Using 3.7 μm saturation as their detection criteria, they found good correspondence with observed smoke plumes. In contrast, Brustet et al. (1991) reported on an AVHRR study in semi-arid West Africa. They found that a threshold in the 3.7 μm channel alone was adequate for fire detection only in some cases, while for dry

vegetation with hot background soil surfaces, a second threshold applied to the 11 μm channel was necessary.

Techniques developed for vegetation fires can also be used in an urban setting as shown by Doussett et al. (1993) through the detection of fires following the Rodney King verdict in Los Angeles in April 1992. Robinson (1991), Kennedy (1992) and Justice and Malingreau (1994) all provide reviews of fire detection with AVHRR and address a number of sources of uncertainty. a broad review and discusses the limitations and problems of fire detection with AVHRR.

3. MODIS STRATEGY FOR REMOTE SENSING OF FIRES

Experience using the AVHRR shows that fire detection and characterization are limited by the sensor saturation, problems in the sensor radiometric response, signal attenuation by atmospheric water vapor and variation of the observation time from one year to another (NOAA 11 drifted by half an hour a year in its observation time). The use of AVHRR active fire information for regional estimates of emissions is also constrained by its limited sampling of the diurnal cycle of fire activity.

The need for better tools in assessing biomass burning from remote sensing led to the inclusion of two fire channels in the Moderate Resolution Imaging Spectroradiometer (MODIS) instrument (Salomonson, 1989), to be flown on the Earth Observation System (EOS) in 1998 (observations at l0:30 am and l0:30 pm local subsatellite time) and 2000 (observations at 1:30 pm and 1:30 am local subsatellite time). In contrast with AVHRR, MODIS will be equipped with infrared (IR) spectral channels specifically designed to detect and characterize fires and their emitted thermal energy. The 4 and 11 μm channels are designed to be sensitive to temperatures reaching 500K and 400K respectively. Therefore, except for large wild fires these MODIS channels, with resolution of 1 km at nadir are not expected to saturate. MODIS is planned to monitor global fire activity twice during the day (after the launch of the second platform) and twice during the night. The main remote sensing effort will be towards accurate detection of the presence of fires and their location, which will be used to monitor the frequency and spatial distribution of fires. In addition, the detected radiation emitted from the fire at 4 μm will be used to monitor the apparent thermal radiation emitted by the fire, which is expected to be proportional to the instantaneous rate of biomass consumption by the fire, and, therefore, to the rate of emission of trace gases and aerosol particles. The

relationship between the fire IR brightness temperature at 4 μm and 11 μm, for fires with signals above the background temperature variability at 11 μm, should be an indication of the average fire temperature, and therefore also of the relative contribution of smoldering (cooler) and flaming (hotter) to the biomass consumption and their effect on the combustion efficiency and emissions. Note that the combustion efficiency is the fraction of carbon released from the biomass in the form of CO2 (Ward et al., 1992). We do not have yet enough experience to judge the acuracy of the rate of emission of thermal radiative energy from the fire. Radiative processes in the fire, spatial nonhomogeneity of the fire pixel and obscuration by vegetation and ash can affect the measurements, but the rate of emission of thermal radiative energy is expected to be useful for comparison between the strength of fires at different locations and times.

Extensive comparison between the fire thermal energy and the emission of smoke in different ecosystems, will enable "calibration" of the measured thermal energy into the emission of smoke trace gases and particulates. The interpretation of the detected fire energy in terms of consumed biomass is difficult and may vary from one vegetation type to another. It will require "calibration" using field or laboratory measurements. The success of the MODIS algorithm and products to separate smoldering and flaming fires or to indicate the combustion efficiency will be "calibrated" using laboratory measurements and validated in the field after launch.

The MODIS instruments alone will provide up to 4 observations in 24 hours. Given the limited sampling of the diurnal cycle, emission estimates may have to be based on a combination of the MODIS high resolution data and geostationary observations of fires, using a coarser spatial resolution but a higher temporal resolution (every half-hour). At this time, coverage from GOES is restricted to the North, Central and South America however, over the next decade, METEOSAT second generation satellites and MTSAT will provide coverage of Europe, Africa, Asia, Australia and the Pacific Islands.

Two additional algorithms are under development as part of the MODIS suite of fire products for early post-launch implementation and testing. Firstly a simplified algorithm for MODIS near real-time volcano and fire alert is being developed by the University of Hawaii as part of a NASA Interdisciplinary Science (IDS) study in conjunction with the MODIS fire team. This alert algorithm provides

an initial filtering of five channels of the data stream and is designed to run at an early stage in the MODIS data chain with no other data dependencies, thus enabling rapid access to the data. The volcano and fire alert products provide the basis for a multistage sampling enabling the coarse resolution targeting of high resolution coverage from ASTER and Landsat 7. Secondly, the MODIS burn scar product is being developed to meet the needs of the emissions modeling community by providing a direct estimate of area burned. The algorithm follows a convergence of evidence approach from the time series data, taking advantage of both the spatial and spectral coverage of the MODIS. Attention is currently being given to the reflectance component of the MODIS 4μm for scar identification,

4. MODIS INSTRUMENT CHARACTERISTICS

The MODIS lkm 4μm high gain channel was specified to have a saturation level of 500K with NEdT of 0.3 K. This channel is not affected by water vapor absorption and only weakly affected by other gaseous absorption (see Fig. 5).

The MODIS 11 μm channel, with a 1 km resolution, saturates at a temperature of 400K, with NEdT of 0.lK. Detection may be also possible at night using the 0.86 μm channel which has a 250 m resolution and 2.1 μm and 1.6 μm channels, with a 500 m resolution, though there are currently no plans for routine collection of the solar channels during the night. The MODIS design tries to ensure the highest possible locational accuracy of the data to provide the best information as to the location of fires and to allow multitemporal monitoring of fires. Good band to band registration (0.1 of a pixel) and scene to scene registration is required, since misregistration will lead to overestimation of fire occurrence. Since there is no possibility for on-board calibration of the fire channels at high temperatures, detailed preflight calibration is planned, as well as in-flight vicarious calibration using known fixed sources e.g. gas flares.

The MODIS 250 m bands can be used to provide information on the spatial variability of the 1 km fire pixel and the background surface. An inverse relationship has been established between the NDVI and surface temperature, which may help with assumptions concerning background temperature. The MODIS cloud mask will be an important component of the fire detection to identify areas where the surface is obscured by clouds and fires are undetectable. The 250 m channels will also be used to detect sub-pixel clouds within the 1 km pixel. The

MODIS sensor scans the Earth with 10 simultaneous 1 km wide stripes (or 20 and 40 stripes at the 500 m and 250 m resolutions respectively). The general design of the MODIS instrument and its application for remote sensing are described in Salomonson et al. (1989); King et al., (1992) and Running et al (1994). At off-nadir there is an overlap between the scan lines of different swaths. To avoid the effect of off nadir viewing on mutiplicative fire detection, we shall limit the fire detection to view angles of ±45°.

The MODIS pixel size at 4 μm and 11 μm is 1 km. However, due to the scanning mode of MODIS the response is triangular across 2 km with maximum response in the center of the pixel (see Fig. 6). As a result, fires can be expected to be detected by one or two adjacent pixels depending on the location of the fire relative to the pixel and on the strength of the fire. Note that if instead of a triangular response, the MODIS response would be rectangular with no overlap, each fire would be singularly detected with a response equal to the sum of the responses of the two adjacent pixels depicted by the triangular response.

5. SPECTRAL PROPERTIES OF FIRES

The MODIS algorithm is based on the spectral properties of fires in the mid and longwave IR. These properties are the result of the fire pixel inhomogeneity and the expected range of the fire temperatures. In a given fire pixel we may have areas that are not burned, areas that are smoldering and areas that are in flames. Figure 7 demonstrates the sensitivity of the potential MODIS channels to the fraction of the pixel covered by flames of 1000K (f_{flame}), and a fraction of the pixel covered by smoldering of 600K (f_{smold}) . The rest of the pixel has a temperature of 300K. The shorter the wavelength, the stronger the sensitivity to the higher temperature region. The main results of the simulation are summarized in Table 2. The 1.65 μm channel is very sensitive to f_{flame} and the flaming energy and not very sensitive to f_{smold} and its energy. The 2.13 μm channel is very sensitive to f_{flame} and somewhat sensitive to f_{smold}. Since the thermal energy is more concentrated in the flaming fire, the sensitivity to thermal energy is independent of smoldering or flaming. Unfortunately the MODIS 2.13 μm channel saturates at a reflectance of 0.8, which for the low solar brightness in this channel corresponds to less than 1% of the 500 m pixel being in flames. During the day this channel is strongly affected by the reflection of sunlight. The importance of this channel is therefore limited. The 4 μm

channel is the next atmospheric window. It is sensitive to both f_{flame} and f_{smold}, and is 5 times more sensitive to the thermal energy emitted from smoldering than from flaming, The stronger sensitivity to smoldering means that for the same apparent temperature in 4 μm, measured by MODIS, the rate of emission of radiative thermal energy and the rate of combustion is higher in the grassland fires than in deforestation fires, that have a much more pronounced smoldering phase (Ward et al., 1992). The reflection of sunlight in this channel is much less important due to the low levels of solar radiation in this channel (at 3.9 μm the sun is half as bright as in 3.75 μm used on AVHRR). It therefore is our main channel for fire detection and characterization. Fig. 8 shows the effect of a fire size and temperature on the apparent temperature of the pixel at 4 μm. This channel is sensitive to fires as small as 10^{-4} of the fire pixel. The 4 μm channel response in daytime may be strongly enhanced by surface reflection where the satellite-surface-solar geometry results in sunglint. This effect has been documented over oceans (Nath et al., 1993; Cracknell, 1993, Setzer and Verstrate, 1994) and can lead to false fire detections over land (Setzer and Malingreau, 1996). Therefore the MODIS fire algorithm tests for sun glint and excludes those pixels from the fire products.

6. MODIS FIRE ALGORITHM

The MODIS fire detection and characterization techniques are planned to be fully automated for the production of daily, global fire information. In order to detect the presence of fire in a non-interactive fashion, a set of detection criteria different for the day and night fire observations are prescribed.

6.1 Fire Detection

The following procedure emerges from the physics of fire thermal emission discussed above and the algorithms used with currently available AVHRR and GOES data. Only the procedures using the 4 μm and 11 μm bands are described. In its current form, a number of threshold values are included. These values are given for both day and night observations. During the night the signal in 4 μm is smaller due to lack of reflection of sunlight and the thresholds are lower. The regional and seasonal variability of the land surface makes absolute thresholds insufficient. The threshold values presented below were subjectively determined, based on the cited literature and the present remote sensing experience of the authors. The value of

the thresholds determines the minimum size and energy of a fire that can be detected. We expect the thresholds to be improved and replaced using analyses of data from airborne instrumentation flown in the Smoke Cloud and Radiation (SCAR) experiments in the US and Brazil.

Fire detection is based on the MODIS signal at 4 μm, and is enhanced by the information at 11 μm. The fire detection strategy is based on absolute detection of the fire, if the fire is strong enough, and on detection relative to the background to account for variability of the surface temperature and reflection of sunlight. To avoid false detection, all pixels for which T4<315K or 305K at night or the difference between the temperature at 4 μm and at 11 μm (dT4l), dT41<5K (3K) are not considered as fires. For a background of 310K at 4 μm, this corresponds to a fire size of 1000 m2 at 600K or 50 m2 at l000K. After launch we shall check if due to this criteria small fires are missed in the Boreal region where surface temperatures are relatively low.

For absolute fire detection the algorithm requires that the fire apparent temperature at 4 μm is T4>320K (315K at night) and dT41>20K (10K at night). But if T4>360K (330K at night), the threshold for dT41 is not required. This may be important for large low temperature smoldering fires that may not have a significant spectral variability in the IR.

If this criterion is not met the algorithm allows a relative fire detection, in which the fire is distinguished from the background by 4 standard deviations in T4 and in the difference dT41:

$$T_4 > T_{4b} + 4\delta T_{4b} \quad \text{and} \quad \Delta T_{41} > \Delta T_{41b} + 4\delta \Delta T_{41b}$$

where sT4b is the standard deviation of the background temperature at 4 μm and sdT41b is the standard deviation of the difference in the background temperature at 4 and 11 μm. sT4b or sdT4lb are kept to be at least 2K.

6.2 Rate of emission of thermal radiative energy

The total rate of emission of radiative energy from the fire, Ef, is expected to depend on the rate of combustion of biomass in the fire. The heat of combustion is divided between conductive/convective heat and radiative heat. Part of the radiative energy is emitted towards the ground and converted to conductive heat in

the ground. Part of the radiative energy may be obscured by cooler material (ash, biomass) above the combustion level. The division between conduction/convection and radiation can be temperature dependent. The reason that we expect the detection of the fire radiative energy to be useful, is that both the rate of emission of radiative energy, and the rate of combustion are proportional to the size of the subpixel fire and to the density of the biomass burned in it. Therefore the rate of emission of radiative energy is expected to represent well the fire intensity and be proportional to the rate of emission of trace gases and particulates from the fire. The ratio between the radiative energy and the total combustion energy may vary between different ecosystems, and presently is not known. Laboratory measurements and experience with MODIS fire products after launch will allow **a** detailed quantification of this parameter. Using MODIS data we shall follow previous analysis of AVHRR data (Kaufman et al., 1990a, b) in which the emission of particulates was associated to **a** given region of fire. While from the AVHRR we were able to relate the emission only to the total number of fires, for MODIS we can relate it to the sum of the fire radiative energy and thus the intensity of the individual fires will be taken into consideration.

The rate of emission of radiative energy, is derived from the measured fire temperature at 4 μm, T4. T4 is defined as the temperature of a blackbody that emits radiance equal to that detected by the satellite in the 4 μm channel. Ef, is correlated to the value of T4 (see Fig. 9a) more than to temperature of any other channel, since this channel is sensitive to both smoldering and flaming (though more to flaming). There is only a small influence from the ratio between smoldering and flaming on the dependence of Ef on T4 (see Fig. 9a). The relationship between the emitted energy and the detected temperature in the 4 μm channel is approximated in Fig. 9a by:

$$E_f = 4.34 \cdot 10^{-19} (T_4^8 - T_{4b}^8) \quad \text{(watt/m2 or MWatt per pixel)}$$

and shown by the solid line. Sensitivity studies and applications of this concept are given in subsequent sections.

6.3 Smoldering and flaming fires

Amongst the fire characteristics planned for estimation using MODIS, the determination of the flaming and smoldering ratio is perhaps the most challenging. The two fire stages: flaming and smoldering, distinct for example in forest fires, are characterized by different fire intensity, temperature, combustion efficiency and emission ratios. In several field experiments in Brazil, Ward et al., measured 2-3 times as much emission of aerosol particles, CH4 and NMHC, per unit of biomass, in the smoldering phase as in the flaming phase (Ward et al., 1992; Kaufman et al., 1992; Malingreau et al. 1993). Therefore it is important to be able to distinguish between these two phases. Figure 10 shows the difference in the emission factors between smoldering and flaming as a function of the combustion efficiency. The data collected in the tropics represent grassland and forest fires. Their emission factors are well represented by a single line as a function of the combustion efficiency. For the particulates there is also a good agreement between the measurements in the tropics and the average relationship obtained for the prescribed fires in North America (Ward and Hardy, 1991). For CH4 there is a substantial difference in the average relationship, that is important in estimate the emissions for combustion efficiency smaller than 0.85.

Smoldering and flaming correspond to different ranges of the combustion efficiency. They can be distinguished using IR remotely sensed measurements only if the fire temperatures vary significantly between these two stages. Based on review of the fire properties by Lobrt and Warnatz (1993), flaming temperature can be anywhere between 800K and 1200K and as hot as 1800K. Smoldering should be under 850K and above 450K. The actual range is probably smaller. Therefore we shall base the algorithm and sensitivity studies on the assumption that the flaming temperature is l000K±200K and smoldering 600K±l00K. Figure 9b shows a simulation of the relationship between the apparent fire temperatures at 11 μm and 4 μm and the fraction of the combustion in the smoldering phase. To distinguish between smoldering and flaming it is required that the fire apparent temperature at 11 μm be significantly larger than the background: dTll=Tl1-Tllb > 2sTllb. In addition, the minimum difference in temperature between the fire pixel and the background should be dT11> 0.5K and dT4=T4-T4b > 10K at 11 μm and 4 μm respectively. The relationship between the apparent temperature at 11 μm and at 4 μm is used to distinguish between 3 possible fire phases, namely only smoldering, only flaming and a mixture of both (see Fig. 9b). To generate a threshold that can be used to distinguish between smoldering and flaming, we used a simulation of

numerous fires with a varying fraction of smoldering and flaming. The average relationship between dT11 and dT4 for all the data is:

$$dT11=0.057dT4^{1.1} \quad (5)$$

and reflects the change in the fire energy. The residue: $sTll = dT11 / (0.0057dT4^{1.1})$ represents the access signal at 11 μm due to smoldering rather than flaming. It is plotted as a function of dT4 in Fig. 11. The residue separates between smoldering, flaming and a mixed zone in between, and therefore is expected to be correlated with the combustion efficiency. The thresholds that separate between smoldering and flaming are derived from:

If sTll < l.0K - flaming stage

If sTll > 1.7K - then smoldering stage

Otherwise - a mixed stage

6.4 Algorithm Components

1. **Cloud detection and scan angle limits:** The fire information is derived for all land pixels but the presence of clouds is determined using the MODIS cloud mask. For example, thick clouds, with reflectance larger than 0.2 in the 0.66 μm channel will be identified as these clouds may not be transparent to the fire signal. The MODIS cloud product includes an assessment of the 250 m channels for the presence of cloud. A scan angle cut-off will be determined to limit problems associated with fire detection and characterization at extreme view angles (e.g. 45").

2. **Atmospheric correction:** The apparent temperatures T4 and Tll, will be corrected for gaseous absorption, including water vapor absorption at 11 μm using the MODIS water vapor products. Note that small clouds may reduce the apparent fire temperature at 11 μm and may impact the derived smoldering/flaming ratio.

3. **Background characterization:** The relationship between the apparent temperatures of the pixel being examined and its surrounding pixels is established. The surrounding pixels are used to estimate the background temperature (or non-burning temperature) of the fire pixel. This approach

assumes that the correlation between the background temperature of the fire pixel and surrounding pixel temperatures decreases with distance from the pixel. An expanding grid centered on the fire pixel is interrogated until a sufficient number of cloud, water or fire free pixels are identified.

Energetic fire pixels are eliminated from the analysis of the characteristics of the background to the fires and are determined as having dT41 = T4 - T11> 20K (10K at night) and T4 > 320K (315K at night). Excluding these energetic fires, the average background apparent temperature - Tllb and its standard deviation - sTllb are calculated. In a similar way T4b and sT4b are calculated. The median temperature difference between 11 μm and 4 μm apparent temperatures of the background as sT41b and the standard deviation as sdT41b are calculated.

4. **Fire detection:** All pixels for which T4<315K (305K at night) or dT41<5K (3K at night) are not considered as fires. If the standard deviations sT4b and sdT41b are less than 2K, use 2K instead. Define a fire pixel (from the remaining pixels) if for this pixel one of the following 5 combinations of logical conditions (labeled by letters) are met:

$$\{[(T_4 > T_{4b} + 4\delta T_{4b}) \text{ or } T4>320K(315K \text{ at night})] \text{ and } [(\Delta T_{41} > \Delta T_{41b} + 4\delta\Delta T_{41b}) \text{ or } \Delta T_{41} > 20K(10K)]\} \textbf{ or } \{T4>360K(330K)\} \quad (1)$$

(A) (B) (a) (b) (x)

5. **Glint exclusion:** exclude a fire pixel during the day if it corresponds to glint measurements: T11<T11b (lakes and rivers are cooler than land) and ~0.6~0.3 and p0.86>0.3 (a reflectance that corresponding to 312K at 4 μm) and glint angle <30°.

6. **Consolidation:** As a result of the triangular response of MODIS (Fig. 6), the same fires may be represented by two adjacent pixels in the scan direction. This will be particularly true for strong fires. Approaches are being developed to consolidate the number of fires after initial detection. One statistical approach currently being evaluated is outlined below and would be implemented for the 10km gridded product. The first step is to determine the total number of fires, Nf, number of pairs or triplets in the scan direction, Ns,

and the number of pairs or triplets in the track direction, Nt. If Ns-Nt > 3 and Ns-Nt > Nf/3 then there is a need for fire consolidation. The detected fires are consolidated in the following way:

i) A single pixel fire detected - no consolidation

ii) 2 adjacent fire pixels detected along-track. Combine the MODIS response for the fires into a single fire detection:

$$L_{4c}=L_{4\alpha}+L_{4\beta}-L_{4b} \quad (2)$$

where the radiance is computed from the Planck function: L4=P(T4), for pixel a and β. The radiance is converted to the combined temperature using the inverse Planck function: $T_{4c}=P^{-1}(L_{4c})$. Same consolidation is applied at 11 μm. L4b is the background radiance at 4 μm.

iii) N adjacent pixels along track detect fires:

$$\begin{aligned} L_{\lambda c1} &= L_{\lambda 1}+\tfrac{1}{2}L_{\lambda 2} \\ L_{\lambda ci} &= \tfrac{1}{2}L_{\lambda i}+\tfrac{1}{2}L_{\lambda i+1} \quad \text{for} \quad 1<i<N-1 \\ L_{\lambda cN} &= L_{\lambda N}+\tfrac{1}{2}L_{\lambda N-1} \end{aligned} \quad (3)$$

The pixel location of the fire is defined by the weighted average of the centers of the pixels, where the weights are the excess radiance at 4 μm.

7. **Total rate of emission of radiative energy from the fire:** The relationship between the emitted energy and the detected temperature difference in the 4 μm channel is approximated by:

$$E_f=4.34\cdot10^{-19}(T_4^8-T_{4b}^8) \quad \text{(watt/m2 or Watt per pixel)} \quad (4)$$

8. **Smoldering or flaming stage:** To distinguish between smoldering and flaming it is required that:

$\Delta T_{11} > 2\delta T_{11b}$, $\Delta T_{11}>2K$ and $\Delta T_4>10K$.

Otherwise only Ef is determined from the average relationship between T4 and Ef. To eliminate the effect of background temperature, the apparent temperatures at 11 μm and at 4 μm are first scaled to a background

temperature of 300K and zero reflectance, by subtracting the excess radiance. The thresholds that separate between smoldering and flaming are derived using:

$$\delta T_{11} = \Delta T_{11} / (0.0057 \Delta T_4^{1.1}): \quad (5)$$

If $\delta T_{11} <$ l.OK - flaming stage

If $\delta T_{11} >$ 1.7K - then smoldering stage

Otherwise - a mixed stage

5.2 Fire Products at Coarser Grids

The fire products will be generated from all the individual observations stored over a 24 hour period at a Level 2 grid. The Level 2 data base will be archived and made available to the user community. The fire products will be assembled for individual days and summarized for cornpositing periods of eight days and one month. Products will be available at full resolution (1 km) as well as for coarser grids at 10 km and 0.5". These latter products are being designed for use in regional and global modeling.

Table 3 summarizes the information collected for individual fires. The information to be stored will include summaries of the actual measured quantities: T4, T11, T4b, T11b, δT_{4b}, δT_{11b}, total emitted energy, Ef, and flaming/smoldering phase detection δT_{11}. Statistics on cloud obscured observations will also be stored. The information is stored separately for each each of the two or four daily fire observations.

The information for a grid box of 10x10 km and 0.5" x. 0.5°, will classify the fires based on their temperature at 4 μm, T4, (which is proportional to the thermal energy) and store the number of fires identified in each class:

Class 0: T4<315K
Class 1: 315K<T4<320K
Class 2: 320K<T4<325K
Class 3: 325K<T4<335K
Class 4: 335K<T4<350K
Class 5: 350K<T4<400K
Class 6: 400K<T4<450K
Class 7: 450K<T4<500K

For each class the average value of $\Delta T_{41}=T_4-T_{11}$ will also be stored as well as the total thermal energy emitted in the grid box and the average ratio smoldering/total, weighted by the total emitted energy.

Current plans are to provide a MODIS burned area product at a 10 km grid on an eight day and monthly basis. The product is targeted at those developing emission inventories. The algorithm is currently under development and comparisons are being made between the use of vegetation indices, surface reflectance, surface temperature and surface texture time-series. Emphasis is also being given to the reflectance component of T4 at 1 km, which shows a marked contrast between burn scars and surrounding unburned areas (Roger et al. 1996). An example of the channel 3 surface reflectance product derived from the NOAA AVHRR is given in Figure **#. (figure showing the scar response in channel 3 - Chris**).

6. SIMULATION STUDIES

Simulations are used to show the sensitivity, expected accuracy and application of the MODIS fire algorithms to synthetic data. The first example given, is a simple simulation of a mixture of smoldering, flaming and background surfaces. Several flaming and smoldering temperatures are used in the simulation, due to the uncertainty in these temperatures: smoldering - 600K±100K and flaming - 1000K ± 200K. The simulation, shown in Fig, 12, is designed to test the possibility of distinguishing between smoldering and flaming conditions from space observations of the spectral apparent fire temperature. The simulation looks for all the possible fire characteristics at the range of temperatures described above, that give the same spectral response at the 4 and 11 μm channels at the satellite sensor. For example, the open circles in Fig. 12, represent fraction of the fire in the smoldering stage between 0 and 40%, and all of them give the same spectral response at 4 and 11 μm of T4=400K and T11=309K. The simulation shows that the total emitted thermal energy can be much more accurately derived from the measurements than the ratio of the thermal energy emitted in the smoldering or flaming stages. The total emitted energy, that corresponds to a given set of measurements varies by only ±10%. The ratio of the energy emitted as smoldering to the total, varies usually by ±20%, which

is sufficiently only to distinguish between three stages of fire: flaming, smoldering or mixed stage. Uncertainty in the assumed temperature of the smoldering and flaming stages are the main sources of uncertainty in the derived fire thermal energy and fractionation between smoldering and flaming components.

An additional source of uncertainty is the background characterization. It is possible that the background temperature to the fire that is found within the MODIS fire pixel is different from the background that MODIS senses outside of the MODIS pixel. This can happen, for example, if part of the MODIS pixel is already on fire before the MODIS pass and still has a warmer temperature and higher or lower reflectance at 4 μm. For the strongest fire in Fig. 12 with Ef=1300 Mwatt, an uncertainty in the background temperature of 5K corresponds to an error in Ef of only 2% and in the fraction of energy released in the smoldering stage of 5%. Similar errors result from uncertainty in the surface reflectance at 4 μm of $\Delta\rho_4$=0.05 for this fire. For fires that consume less biomass and radiate less energy it is more difficult to determine the total emitted energy and fraction of energy emitted in smoldering. For the second smallest fire in Fig. 12, with Ef=230 Mwatt, the apparent temperature of the fire pixel at 11 μm is only 9K more than the background. In this case if the background temperature is underestimated by 5K, the energy of the fire will be overestimated by 15% and instead of considered as pure flaming, the fire is considered as mixed phase. For the weakest fire in Fig. 12, smoldering or flaming cannot be determined in the presence of such uncertainties in the background temperature or reflectance, but the error in total energy is only 15% for an error in background temperature of 5K. Therefore it is concluded that uncertainties in the background reflectance and temperature can be tolerated in the derivation of the fire emitted energy but it is possible to distinguish between smoldering and flaming only if the response of the temperature at 11 μm, ΔT_{11}, is at least twice as large as the uncertainty in the background temperature. The mid-IR 500 m resolution reflectance observations will be used to determine the heterogeneity of the fire pixel and the difference between the fire pixel and the background. It will be used as part of a quality flag. The larger the heterogeneity, the larger is the effect of background uncertainty on the determination of flaming and smoldering ratios.

The second simulation addresses the large spatial heterogeneity of fires. Each fire pixel was subdivided into 500 zones. The temperature of these zones is defined by 3 main temperatures: background, Tb, smoldering, Ts, and flaming, Tf, but each

zone is assigned randomly a temperature in a Gausian distribution around one of these three temperatures, with a fixed predetermined fraction of smoldering and flaming in the fire pixel. By varying the values of Tb within 280-320K, Ts within 400-600 and Tf within 700-1300, and varying the width of the distributions, we obtain a variety of conditions that simulate the natural variability. The simulation was performed using Excel with Macro programming for 150 fire pixels, each with a different average temperature and coverage of the smoldering and flaming fires. For each pixel the "true" fire energy was calculated by summing the excess energy in the 500 sub-units. The total radiometric response at 4 μm and 11 μm was also calculated and used in the empirical eq. 4 to calculate the apparent fire thermal energy. Fig. 13 shows a comparison between the true and retrieved apparent fire energy. The retrieved fire energy fits the true energy very well. The average standard deviation in deriving the fire energy is 16%. It is larger for small fires and smaller for energetic fires (see Table 5). Inclusion of an uncertainty in surface reflectivity of sunlight between the background 'and the fire pixel, generated negligible errors in the derived energy for energies larger than 100 MWatt. The error was larger for smaller fires. Table 5. Summarize, the results.

7. MODIS Fire Product Prototyping activities: auulication to wild and prescribed fires

7.1 Landsat observations of the 1988 Yellowstone Fire

The Yellowstone fire in Wyoming, Montana, and Idaho began with a series of lightning strikes on July 9 - 11, 1988 and eventually spread to engulf 5,000 km2 in and around Yellowstone National Park. (Morrison, 1992). A Landsat TM image was collected on September 8, 1988 at 10:30 AM and is used here to describe the wildfire and to simulate MODIS fire observations. The Landsat TM imager has 7 spectral channels, six with a resolution of 30 m: 0.48 μm, 0.56 μm, 0.66 μm, 0.83 μm, 1.65 μm, and 2.2 μm and one with a resolution of 120 m at 11.4 μm. Figure 14 shows the entire Yellowstone data set (216 km x 180 km) resampled to 500 m/pixel spatial resolution and converted to simulate MODIS bands 7 (red, 2.2 μm), 6 (green, 1.65 μm), and 1 (blue, 0.66 μm). The image is particularly useful for identifying a chronology of fire activity. Pink areas are regions of intense active fires, while brick-red areas represent burn scars that are 1 to 3 days old where smoldering elements and small fire pockets are still radiating significant amounts of flux at 2.2 μm. Older burn scars are included in the yellow areas of the image. Thus, MODIS channels 7, 6, and 1 could be used to estimate the extent of active fires and recent burn scars while smoke enshrouds the area of interest.

As a background to the satellite observations, we shall describe the fire development of the preceding day for a small subsection of Yellowstone (Figures 15 and 16, see also Flynn and Mouginis-Mark, 1995). Twenty-four hours before the TM pass there were two large columns of smoke and fire 5 km west and southwest of the location of the Yellowstone Old Faithful geyser. At 3 PM on September 7, the winds began to strengthen from the southwest. At 3:30 PM, the fire was close to the Old Faithful Visitor Center with strong enough convection to generate winds of 80 km/hr towards the fire. Fire balls and flaming elements passed to the northeast of the visitor center (Morrison, 1992). That particular fork of the fire zone (shown 20 km west of Yellowstone lake in Figure 10) grew by 200 km2 that day .

Figure 15a is a false color composite of the 11.4 μm (red), 2.2 μm (green), and 1.65 μm (blue) TM channels which shows the location of the fire and the burned area. The burn scars are warmer than the surrounding area and are therefore, shown in pink-red colors. The large burn scar in the lower right part of the image was generated by a fire storm 19 hours before the acquisition of the TM image. It is 2.1 km wide at the base and 12.7 km long. Many of the active fires located mainly along the perimeter of the burn scar saturated the 2.2 μm channel. The active fire cells appear yellow-white in the image and are relatively small (60 - 120 m) with the largest one 300 m across. Table 6 gives the typical values of reflectance at 1.6 μm and 2.1 μm and temperature at 11 μm of the yellow-white fire spots, the burn scar, and the background. Figure 15b is a composite of the 11.4 μm (red), 0.66 μm (green), and 0.48 μm (blue) channels, showing the position of the burn scars relative to the smoke plumes generated from the more intense fires. Comparison of the two figures shows the relationship between the presence of main fires and the emission of smoke.

Figure 16 shows another simulation of the MODIS response to the Yellowstone fire. Since the TM does not have a 3.96 μm channel which is the main fire channel on MODIS, we-generated it from the non-saturating TM channels (1.65 μm, 2.2 μm, and 11.4 μm). The figure shows on the left a false color composite of the 11.4 μm (red), 3.96 μm (green), and 1.65 μm (blue) in full TM resolution. On the right the same color picture is shown but after the resolution was reduced to 1 km. The same spatial distribution of the information is seen, though it is intuitively less clear due to the reduced resolution.

Quantitative comparison between the rate of emission of thermal energy derived from the simulated MODIS observations and the Landsat observations are shown in Figure 17. The thermal energy is derived from the simulated 3.96 μm channel in both cases using Eq. 4. For the TM, the thermal energy was derived from individual 30 m pixels and averaged to the 1 km resolution. The thermal energy derived from the simulated

MODIS image is plotted in the figure as a function of the thermal energy derived from the TM image. In Fig. 17a the MODIS data are for a hypothetical rectangular 1 km response, and in Fig. 13b for the actual MODIS instrument response (Dr. Kai Yang, personal communication, 1996) which takes into account the geometric distortion of off-nadir pixels. The plots in Fig. 17 show the effect of the reduced MODIS resolution on the detection of fires and the derivation of thermal energy. The reduced resolution retains the basic information of the thermal energy with a difference of less than 1% for fire pixels. Note, however, that there are differences between the "square" 1 km resampled pixels (Figure 13a) and the geometrically distorted pixels (Figure 17b), because in the latter case, the off-nadir fire pixels are larger than those in the former case. Thus, for a given pixel, the fire energy is spread out over a larger pixel in Figure 17b leading to lower fire energies.

The conclusion from this application of the MODIS concept to Yellowstone fire is that this type of wildfire will be clearly observed from MODIS and that the thermal energy can be calculated from the MODIS pixel with a high degree of accuracy. This is another example that shows that the database of MODIS thermal energy can be very useful for comparison between fires but cannot be used in an absolute sense unless correlated with some additional quantity, such as the emission of burning products. This is the subject of the next application.

7.2 MODIS Airborne Simulator data of prescribed fires in the SCAR-C experiment

The SCAR-C (Smoke Cloud and Radiation - California) experiment was conducted in September 1994 in the Northwest US (Kaufman et al., 1996). In the experiment, the entire process of biomass burning was measured, including ground-based estimates of fuel consumption, airborne sampling of the smoke aerosol and trace gases, and air-borne and spaceborne remote sensing of both the fires and the smoke. In this simulation study we use remote sensing data collected during the experiment by the MODIS Airborne Simulator (MAS) flown on NASA's ER-2 aircraft, to find if there is a relationship between the fire emission of thermal energy and emission of smoke and trace gases. The MAS scans in the crosstrack direction in 35 km swaths collecting data with a nominal **45** m resolution **(King reference describing MAS).** For SCAR-C, MAS was configured with 11 spectral channels that included the 0.66 μm, 1.6 μm and 4 μm channels used in this study. Several prescribed and wild fires were measured. The Quinault prescribed fire on the coast

of Washington State (Sept. 21, 1994) was the best measured example of the relationship between the fire rate of emission of thermal energy and the rate of emission of particulates. Both the fire thermal energy and emission of particulates were remotely sensed by MAS. Fire thermal energy was monitored by the 1.6 μm and 4 μm channels, while emissions of smoke were measured independently, in 0.66 μm downwind from the fire. The fuel that fed the Quinault fire consisted of the dry remnants of large western red Cedar debris, left over from logging. The density of the fuel, including the deep forest floor of accumulated woody material, was 38 kg/m2, about half of it (22 kg/m2) was consumed in the burn according to US Forest Service report. The burn site was reported by the US Forest Service to be 0.2 km2, while remote sensing at 4 μm found a similar size of 0.25 km2. The fire was ignited by heliotorch at 18:10 GMT and immediately burned vigorously, continuing for about 6 hours.

The ER-2 flew over the fire eight times, each time generating an image of the size and apparent temperature of the fire and an image of the smoke plume. Fig. 18 shows the first of such remote sensing images taken from the ER-2 of the fire temperature and the emitted smoke. The size of the fire was monitored using the 4 μm channel which proved to be the most sensitive to the temperature anomaly. However, this channel saturated at 450K. As a result, at the MAS resolution the fire thermal energy was monitored by a combination of the 4 μm channel and the 1.6 μm channel. Since the 1.6 μm is sensitive only to temperatures above 620K, there is a gap between the two channels with low sensitivity. The 1.6 μm channel saturates at 860K. For the high spatial resolution of the imagers, this channel is very sensitive to the presence of flaming and gives a high resolution image of the fire. The use of the 1.6 μm channel is different from that of the MODIS 4 μm channel, but demonstrates the application of the use of rate of emission of thermal energy derived from remote sensing. This channel was calibrated on the ground before flight, and the calibration was compared and updated using simultaneous AVIRIS data.

Application of the MAS images of the fire and smoke acquired in the Quinault fire are shown in Fig. 19. The figure shows the rate of emission of thermal energy from the fire and the rate of emission of particulates. The rate or emission of thermal energy is calculated from the difference between the detected radiance at 1.6 μm, and the radiance due to reflection of sunlight. It is converted to the rate of

emission of thermal energy assuming that each 45 m pixel is a homogeneous black body. To calculate the rate of smoke emission, we followed the procedure of Fraser et al. (1984) developed for the calculation of the flux of sulfate exiting the US coast to the Atlantic. The average smoke brightness at 0.66 μm was converted into the smoke optical thickness using a radiative transfer lookup table that describes the relationship between the optical thickness and the upward radiance at the top of the atmosphere for a plane parallel smoke model (Kaufman et al., 1996). The smoke optical thickness (τ) was converted to the smoke mass density (M) using a conversion factor of ζ=0.11 g/m2 for. the dry part of the smoke ($M=\zeta\tau$, Kaufman et al., 1990a). The rate of emission was calculated for an average wind speed of 7±2 m/s. The wind speed was obtained from 6 consecutive observations from the MAS images of the distance of the edge of the smoke plume from the fire. Figure 19 shows that the rate of emission of smoke and the rate of emission of thermal energy, evolve as a function of time in a remarkably similar way. This shows that at least in the case of this fire, there is a direct relationship between the rate of emission of thermal radiation from the fire and the rate of emission of smoke. We plan to apply this procedure to the rest of the fires measured during the SCAR-C experiment and to hundreds of fires in Brazil measured during the SCAR-B experiment in 1995. We also plan to use indoor laboratory fires to establish, in a controlled environment the relationship between the fire thermal energy and rate of emission of aerosol and trace gases.

7.3 AVHRR prototyping of MODIS global active fire products.

The IGBP Global lkm Project provides an important prototype for MODIS data products and is described by Townshend et al (1995) and Eidenshink et al (1995). Data are being collected from a number of ground stations around the World and contributed to a global archive. As part of the NASA EOS program the global daily AVHRR data have been compiled at the Eros Data Center from April 1992 to the present. The daily orbits can be processed to identify fires and can be combined to show the global distribution of fires. **Figure 20 shows the AVHRR distribution of fires for one day in 1992 generated by the GIMMS group at NASA/GSFC. The** image was derived from # individual orbits of data. The IGBP-DIS has a Fire Working Group which is developing a community consensus AVHRR algorithm to be applied to one year of daily fire data due for completion in late 1997. The algorithm is described in Justice and Dowty (1994). The resulting data set will provide a useful

tool to evaluate the global distribution and timing of fires to be identified by the MODIS. It is important to note that several of the limitations of the AVHRR for fire sensing described above will be overcome by the MODIS instrument.

8. CONCLUDING REMARKS

The MODIS fire products are expected to provide a new tool for the monitoring of global fires, and detection of changes in the location, density and rate of biomass consumption of fires over the globe. For large fires, for which the response in 11 μm is significantly above background, MODIS should be able to distinguish between smoldering stage and new flaming stages. This may be important for observations of the behavior of wild fires. While the AVHRR provides observations of the fire distribution in different ecosystems around the World, it is limited in the provision of quantitative information due to the saturation and folding .of the 317 μm channel (Setzer and Verstrate, 1994). The MODIS instrument will be launched with two special non-saturating fire channels. The four MODIS fire observations, after the launch of the second EOS platform in 2000, will be combined with MODIS monitoring of global land vegetation, burn scars, clouds and smoke, and with a full diurnal cycle of fire and smoke observations derived from geostationary satellites. This remote sensing system is expected to yield a complete characterization of the biomass burning process and its effect on land properties, atmospheric chemistry and quality and climate change. MODIS will generate daily, 8 day and monthly composites of fire statistics. In addition to the fire occurrence and location, the thermal signature will be used to detect the apparent radiative thermal energy emitted from the fire and provide a rough estimate of the ratio between the energy partition between smoldering and flaming. We know that the remotely sensed thermal energy is proportional to the rate of consumption of biomass in the fire, a parameter that is useful for estimating the magnitude of biomass burning. But we still need to quantify the relationship between them. The spatial distribution of the fire temperature in the MODIS pixel and obstruction of the radiative flux would affect this relationship as will the distribution of material in the fire bed with its effect on the competition between radiation and conduction/convection in redistributing the thermal energy. We do expect that these properties will be repeated between similar ecosystems and that therefore it will be possible to establish the empirical relationship between the remotely sensed thermal energy and the emission of particulates and trace gases from the fire.

Establishing this relationship would be a major advance from the estimation of the average amount of particulates emitted per fire derived from the AVHRR (Kaufman et al., 1990a). Before the launch of MODIS these relationships will be established in laboratory measurements that simulate fires from different ecosystems.

The recent SCAR field experiments, in the Northwest US and in Brazil using an aircraft version of the MODIS instrument have started to establish these basic relationships and to test the MODIS algorithms. In the remaining time before launch in 1998 we plan to continue with controlled laboratory experiments and aircraft data analysis. In the post-launch period, emphasis will be given to product evaluation and conducting additional field experiments in a variety of ecosystems. One such campaign is currently being planned for Southern Africa in 1999.

Table 1: The AVHRR operational fire count of INPE during 1992-1995. The data for 1995 are given till Aug 17, before a change to a late satellite with a non-representative fire count.

period of time	number of AVHRR fire pixels
June 1991	6,000
July 1991	18,000
August 1991	210,000
September 1991	214,000
October 1991	20,000
June-October 1991	470,000
June-October 1992	**290,000**
June-October 1993	315,000
June-October 1994	**117,000**
June-Aug 17 1995	**123,000**

Table 2 Information on the MODIS bands that can be used for fire detection. The saturation is given in reflectance units for the solar bands (ρ) or in temperature units (T) for the thermal bands. The sensitivity is given in degrees change (AT) per change in the area covered by fire (f) or in change in the apparent surface reflectance ($\Delta\rho$).

:hannel	spatial resolution	saturation	fraction of pixel that saturates the channel at 1000K	at 600K	sensitivity ($\Delta T/\Delta f$) and ($\Delta T/\Delta E_f$) of smoldering at 600K	sensitivity ($\Delta\rho/\Delta f$) and ($\Delta\rho/\Delta E_f$) of flaming at 1000K
1.65 µm	500 m	ρ=1 (740K)	0.05	no saturation	$\Delta\rho/\Delta f$=0.064 $\Delta\rho/\Delta E_f=9\cdot10^{-6}$	$\Delta\rho/\Delta f$=220 $\Delta\rho/\Delta E_f=5\cdot10^{-4}$
2.13 µm	500 m	ρ=0.8 (570K)	0.007	0.65	$\Delta\rho/\Delta f$=1.2 $\Delta\rho/\Delta E_f=2\cdot10^{-4}$	$\Delta\rho/\Delta f$=110 $\Delta\rho/\Delta E_f=3\cdot10^{-4}$
4 µm	1000 m	500K	0.025	0.30	$\Delta T/\Delta f$=800 $\Delta T/\Delta E_f$=0.11 at f=0.05	$\Delta T/\Delta f$=8300 $\Delta T/\Delta E_f$=0.02 at f=0.005
11 µm	1000 m	400K	0.07	0.25	$\Delta T/\Delta f$=480 $\Delta T/\Delta E_f$=0.07 at f=0.05	$\Delta T/\Delta f$=1700 $\Delta T/\Delta E_f$=0.004 at f=0.005
energy, E_f (MWatt)					**$\Delta E_f/\Delta f$=7300**	**$\Delta E_f/\Delta f$=430,000**

Table 3: Quantities to be archived for individual fires from the *MODIS data.*

Type of information	Quantities
location of the fire pixel	latitude and longitude
measured quantities	T_4, T_{11}
background quantities	T_{4b}, T_{11b}, δT_{4b}, δT_{11b}
logical condition met	logical condition
inverted quantities	emitted energy smoldering/ total ratio

Table 4: Typical reflectance and temperature characteristics of the Yellowstone fires

Wavelength	Fire Condition	Reflectance	Temuerature (K)
1.65 pm	active fire	0.503	
	burn scar	0.139	
	background	0.122	
2.2 pm	active fire	0.913	
	burn scar	0.188	
	background	0.067	
11 pm	active fire		325
	burn scar		317
	background		303

Table 5: Summary of simulation of retrieving the fire thermal energy in the presence of *heterogeneity of the fire temperature.* 150 *fire pixels were simulated with varying fraction of moldering* and *flaming and varying temperatures. Each fire pixel was divided into 500 zones with temperature* chosen *randomly* in a *Gausian distribution around the flaming, smoldering or background temperatures.*

range of fire energy (MWatt)	average energy for the range (MWatt)	relative error (%) with surface reflectance ρ_{back}=0.1, ρ_{fire}=0.05,	relative error with no surface reflectance
12-1200	218	1 6	1 7
12-50	29	38	37
50-100	73	16	19
100-200	142	12	13
200-500	290	9	9
500-1200	643	7	7

Table 6 Typical reflectance and temperature characteristics of the Yellowstone fires

Wavelength	Fire Condition	Reflectance	Temperature (K)
1.65 μm	active fire	0.503	
	burn scar	0.139	
	background	0.122	
2.2 μm	active fire	0.913	
	burn scar	0.188	
	background	0.067	
11 μm	active fire		325
	burn scar		317
	background		303

Acknowledgments.

The authors wish to thank B.-C., Gao for his recommendation for the spectral location of the MODIS fire channel, R. Kleiman, B.-C. Gao, R.-R. Li, A. Chu and L.Giglio contributed calculations and valuable comments to the manuscript. Material from the IGBP-DIS Fire Algorithm Workshop Report contributed to the background information in this paper.

REFERENCES **Bold are not in text**

Andreae M.O., Fishman J., Garstang M., Goldammer J.G., Justice C.O., Levine J.S., Scholes R.J., Stocks B.J. and Thompson A. M. 1994. Biomass burning in the global environment: first results from the IGAC/BIBEX Field Campaign STARE/TRACE-A/SAFARI-92. In: Global Atmospheric-Biospheric Chemistry. Ed. Prinn R, Plenum Press, New York, 83-101.

Belward, A.S., P.J. Kennedy and J-M. Gregoire, 1993, The limitations and potential of AVHRR GAC data for continental scale fire studies, Int. T. Remote Sensing, (submitted).

Brustet, J.M., J.B. Vickos, J. Fontan, K. Manissadjan, A. Podaire, and F. Lavenu, 1991, Remote Sensing of Biomass Burning in West Africa with NOAA-AVHRR, In.:

Global Biomass Burning, Joel S. Levine (ed.), The MIT Press, Cambridge, Massachusetts, pp.47-52.

Cahoon, D.R., Jr., J.S. Levine, W.R. Cofer III, J.E. Miller, P. Minnis, G.M. Tennille, T.W. Yip, B.J. Stocks, and P.W. Heck, 1991, The Great Chinese Fire of 1987: A View from Space, In: Global Biomass Burning, Joel S. Levine (ed.), The MIT Press, Cambridge, Massachusetts, pp.61-66.

Cracknell, A.P., 1993, A method for the Correction of Sea Surface Temperatures derived from satellite thermal infrared data in an area of Sunglint, Int. T. Remote Sensing, 14:3-8.

Crutzen, P.J., L.E. Heidt, J.P. Krasnec, W.H. Pollock, and W. Seiler, 1979, Biomass burning as a source of atmospheric gases: CO, H2, N20, NO, CH3C1, and COS, Nature, 282:253-256.

Crutzen, P. J. and M. O. Andreae, 1990, Biomass burning in the tropics: impact on atmospheric chemistry and biogeochemical cycles, Science, 250:1669-1678.

Dickinson, R.E., 1993, Effect of fires on global radiation budget through aerosol and cloud properties, In: Fire in the Environment: The Ecological, Atmospheric, and Climatic Importance of Vegetation Fires, P.J. Crutzen and J.G. Goldammer (eds.), John Wiley & Sons, New York, pp. 107-122.

Dousset, B., P. Flament and R. Bernstein, 1993, Los Angeles Fires Seen from Space, EOS Transactions, American Geophysical Union, 74(3):33-38.

Dozier, J., 1981, A method for satellite identification of surface temperature fields of subpixel resolution, Remote Sensing: of Environment, 11:221-229.

Flannigan, M.D., 1985, Forest Fire Monitoring Using the NOAA Satellite Series, M.S. Thesis, Department of Atmospheric Sciences, Colorado State University, Fort Collins, Colorado, 59.

Flannigan, M.D. and T.H. Vonder Haar, 1986, Forest fire monitoring using NOAA satellite AVHRR, Canadian Journal of Forest Research, 16:975-982.

Flynn, L. P., and P. J. Mouginis-Mark, 1995, A comparison of the thermal characteristics of active lava flows and forest fires, Geophys Res Lett, 22:2577-2580.

Fraser, R.S., Y.J. Kaufman and R.L. Mahoney, 1984, Satellite measurements of aerosol mass and transport, J. Atmos. Environ., 18:2577-2584.

Hansen J.E. and A.A. Lacis, 1990, Sun and dust versus greenhouse gases: an assessment of their relative roles in global climate change, Nature, 346: 713-719.

Hao, W.M. and M.-H. Liu, 1994, Spatial and temporal distribution of tropical biomass burning, Global Biog. Cycles, 8:495-503.

Hobbs, P.V. and L.F. Radke, 1969, Cloud condensation nuclei from a simulated forest fire, Science, 163:279-280.

IPCC Climate Change 1994, Eds: J.T. Houghton, L.G. Meira Filhno, J.B. Hoesung Lee, B.A. Callander, E. Haites, N. Harris, and K. Maskell, Cambridge University Press, Cambridge. 1995.

Justice C.O., J.D.Kendall, P.R.Dowty and R.J.Scholes, 1996. Satellite remote sensing of fires during the SAFARI campaign using NOAA advanced very high radiometer data, J. Geophys. Research (in press)

Justice, C. O., J.-P., Malingreau, and A. W. Setzer, Satellite remote sensing of fires; potential and limitations, in *Fire in the* Environment, edited by P. J. Crutzen. and J.G. Goldammer, pp.77-88, John Wiley and Sons Ltd., 1993

Kaufman, Y.J. and T. Nakajima, 1993, Effect of Amazon smoke on cloud microphysics and albedo-analysis from satellite imagery. J. Applied Meteorology, 32:729-744.

Kaufman, Y.J., A. Setzer, C. Justice, C.J. Tucker, M.C. Pereira and I. Fung, 1990a, Remote Sensing of Biomass Burning in the Tropics, In: Fire in the Tropical

Biota: Ecosystem Processes and Global challenges, J.G. Goldammer (ed.), Springer-Verlag, Berlin, 371-399.

Kaufman, Y. J., C. J. Tucker and I. Fung, 1990b, Remote Sensing of Biomass Burning in the Tropics, Journal of Geonhvsical Research, 95(D7):9927-9939.

Kaufman, Y. J., and R. S. Fraser,1996, Effect of smoke on increase in cloud reflectivity - remote sensing over the Amazon forest and the Cerrado, submitted to JGR. Dec 95

Kaufman, Y. J., A. Setzer, D. Ward, D. Tanre, B. N. Holben, P. Menzel, M. C. Pereira and R. Rasmussen, 1992, Biomass Burning Airborne and Spaceborne Experiment in the Amazonas (BASE-A). J. Geophysical Res., 97:14581-14599.

Kaufman, Y. J. , B. N. Holben, D. Tanre and D. Ward, 1994,Remote Sensing of Biomass Burning in the Amazon, Special issue on Remote Sensing of the Amazon in Rem. Sens. Rev., 10:51-90.

Kendall J.D,. Justice CO. , Dowty P.R., Elvidge C.D. and Goldammer J.G. (1996). Remote Sensing of Fires in Southern Africa during the SAFARI 1992 Campaign. In: Goldammer J.G. (Ed) The SAFARI Experiment . (in press)

Kennedy, P.J., 1992, Biomass burning studies: the use of remote sensing, Ecological Bulletins, 42:133-148.

King, M. D., Y.J. Kaufman, P. Menzel and D. Tanre, 1992, Remote Sensing of Cloud, Aerosol, and Water Vapor Properties from the Moderate Resolution Imaging Spectrometer (MODIS), IEEE J. Geosc. and Rem. Sens., 30:2-27.

King, M. D., W. P. Menzel, P. S. Grant, J. S. Myers, G. T. Arnold, S. E. Platnick, L. E. Gumley, S. C. Tsay, C. C. Moeller, M. Fitzgerald, K. S. Brown and F. G. Osterwisch, 1996: Airborne scanning spectrometer for remote sensing of cloud, aerosol, water vapor and surface properties. J. Atmos. Oce-anic Technol., 13, 777-794.

Langaas, S. and K. Muirhead, 1988, Monitoring bushfires in West Africa by weather satellites, Presented at the 22nd International Symposium on Remote Sensing of Environment, October 20-26, Abidjan, Cote d'Ivoire.

Lee, T. F. and P. M. Tag, 1990, Improved Detection of Hotspots using the AVHRR 3.7-μm Channel, Bulletin of the American Meteorological Society, 71(12):1722-1730.

Lobert, J.M., and J. Warnatz, 1993, Emissions from the combustion process in vegetation, In: Fire in the Environment: The Ecological, Atmospheric, and Climatic Importance of Vegetation Fires, P.J. Crutzen and J.G. Goldammer (eds.), John Wiley & Sons, New York, pp. 15-38.

Malingreau, J.P., et al., 1995 in- Fire in the environment, P.J. Crutzen and J.G. Goldammer Eds, Wiley, England, 1993?.

Matson, M. and J. Dozier, 1981, Identification of subresolution high temperature sources using a thermal IR sensor, Photo. Ener. and Remote Sensing, 47(9):1311-1318.

Matson, M. and B. Holben, 1987, Satellite detection of tropical burning in Brazil, Int. J. Remote Sensing, 8(3):509-516.

Matson, M., S.R. Schneider, B. Aldridge and B. Satchwell, 1984, Fire Detection Using the NOAA-Series Satellites, NOAA Technical Report NESDIS 7, 34.

Matson, M., G. Stephens and J. Robinson, 1987, Fire detection using data from the NOAA-N satellites, Int. J. Remote Sensing, 8(7):961-970.

McClain, E.P., W.G. Pichel and CC. Walton, 1985, Comparative Performance of AVHRR-Based Multichannel Sea Surface Temperatures, Journal of Geophysical Research, 90(C6):11587-11601.

Menzel, W.P., and E.M. Prins, 1996: Monitoring biomass burning with the new generation of geostationary satellites. Accepted for publication in Biomass Burning and Global Change, J.S. Levine (Ed.), Cambridge MA, The MIT Press.

Morrison, M., 1993, Fire in Paradise, HarperCollins, New York, 253 p.

Muirhead, K. and A.P. Cracknell, 1984, Identification of gas flares in the North Sea using satellite data, Int. J. Remote Sensing 5(1):199-212.

Nath, A. Narendra, M.V. Rao and K.H. Rao, 1993, Observed high temperatures in the sunglint area over the ocean. International Journal of Remote Sensing, 14(5):849-853.

Penner, J. E., R. E. Dickenson, and C. A. O'Neill, 1992: Effects of aerosol from biomass burning on the global radiation budget. Science, 256:1432-1434.

Pereira, M.C. and A.W. Setzer, 1993, Spectral characteristics of deforestation fires in NOAA/AVHRR images, Int. J. Remote Sensing, 14(3):583-597.

Pereira, A.C. Jr., A.W. Setzer and J.R. dos Santos, 1991, Fire Estimates in Savannas of Central Brazil with Thermal AVHRR/NOAA Calibrated by TM/Landsat, Presented at the 24th International Symposium on Remote Sensing of Environment, Rio de Janeiro, Brazil, 27-31 May 1991.

Prins, E. M. and W.P. Menzel, 1992, Geostationary satellite detection of biomass burning in South America, Int. T. Remote Sensing, 13:2783-2799.

Prins, E.M. and W.P. Menzel, 1994, Trends in South American biomass burning detected with the GOES visible infrared spin scan radiometer atmospheric sounder from 1983 to 1991, J. Geoph. Res, 99:16719-16735.

Prins, E.M., and W.P. Menzel, 1996a: Investigation of biomass burning and aerosol loading and transport utilizing geostationary satellite data. Accepted for publication in Biomass Burning and Global Change, J.S. Levine (Ed.), Cambridge MA, The MIT Press.

Prins, E.M., and W.P. Menzel, 1996b: Monitoring biomass burning and aerosol loading and transport from a geostationary satellite perspective. Seventh

Symposium on Global Change Studies, Atlanta, GA, Jan.28 - Feb.2, 1996, pp. 160-166.

Robinson, J M., 1991, Problems in global fire evaluation: Is remote sensing the solution?, In: Global Biomass Burning, MIT Press, Joel S. Levine (ed.), Cambridge, USA, 67-73.

Roger J. C and E. F. Vermote 1996.Computation and use of the reflectivity at 3.75 microns from the AVHRR channels. Remote Sensing of the Environment (submitted).

Running, S.. W., C.O. Justice, V. Salomonson, D. Hall, J. Barker, Y.J. Kaufman, A.H. Strahler, A.R. Huete, J.P. Muller, V. Vanderbilt, Z.M. Wan, P. Teillet and D. Carneggie, 1994,Terrestrial remote sensing science and algorithms planned for EOS/MODIS, Int. J. Rem. Sens., 15: 3587-3620.

Salomonson V.V., W.L. Barnes, P.W. Maymon, H.E. Montgomery and H. Ostrow, 1989, MODIS: Advanced Facility Instrument for Studies of the Earth as a System, IEEE Trans. on Geosc. and Rem. Sens., 27:145-153.

Skole D., B. Moore, W. Chomentowski, 1994. Spatial analysis of land cover change and carbon flux associated with biomass burning in Brazil 1970-1980. In R. Zepp (Ed), Climate biosphere interaction. John Wiley and Sons, NY. 161-202.

Scholes R.J., D Ward and C.O. Justice, 1996, Emissions of trace gases and aerosol particles due to biomass burning in southern hemisphere Africa - J. Geophys. Research (in press).

Setzer, A.W. Operational satellite monitoring of fires in Brazil. International Forest Fire News, FAO-UN, (9):8-11, 1993.

Setzer, A.W.; Malingreau, J.P. AVHRR monitoring of vegetation fires in the tropics: towards a global product. In Biomass Burning and Global Change, ed. J.S.Levine, chap.3, MIT Press, 48-81, in press, 1996.

Setzer, A. W. and M. C. Pereira, 1991, Amazonia Biomass Burnings in 1987 and an Estimate of Their Tropospheric Emissions, Ambio, 20(1):19-22.

Setzer, A.W., and M.M. Verstraete, 1994: Fire and glint in AVHRR's channel 3: A possible reason for the non-saturation mystery. Int. T. Rem. Sens., 15:711-?

Shea R.W., B.W. Shea, J.B.Kauffman, D.E. Ward, C.J.Haskins and MC. Scholes, 1996. Fuel biomass and combustion factors associated with fires in savanna ecosystems of South Africa and Zambia, T. Geouhvs. Research (in press).

Skole, D., B. Moore, W. Chomentowski, 1994. Spatial analysis of land cover change and carbon flux associated with biomass burning in Brazil, 1970-1980. In. R. Zepp (Ed) Climate biosphere interaction. John Wiley and Sons, NY., 161-202.

Stephens, G. and M. Matson, 1989, Fire Detection Using the NOAA-N Satellites, Presented at the 10th Conference on Fire and Forest Meteorology,, April 17-21, Ottawa, Canada.

Thompson A. 1996. Biomass burning and the atmosphere: accomplishments and research opportunities. Atmospheric Environment 30, 19, i-ii

Thompson et al 1996.

Ward, D.E., R. Susott, J. Kauffman, R. Babbitt, B. N. Holben, Y.J. Kaufman, A. Setzer, R. Rasmussen, D. Cumming and B. Dias, 1992: Emissions and burning characteristics of biomass fires for cerrado and tropical forest regions of Brazil - BASE-B experiment', J. Geophys. Res., 97: 14601-14619.

Ward, D.E., W.M. Hao, R.A. Susott, R. Babbitt, R.W. Shea, J. B. Kauffman and C.O. Justice, 1996: Effect of fuel composition on combustion efficiency and emission factors for African savanna ecosystems, J. Geophys. Res., 101, 23569-23576..

Warner, J., and S. Twomey, 1967: The production of cloud nuclei by cane fires and the effect on cloud droplet concentration. J. Atmos. Sci., 24: 704-706.

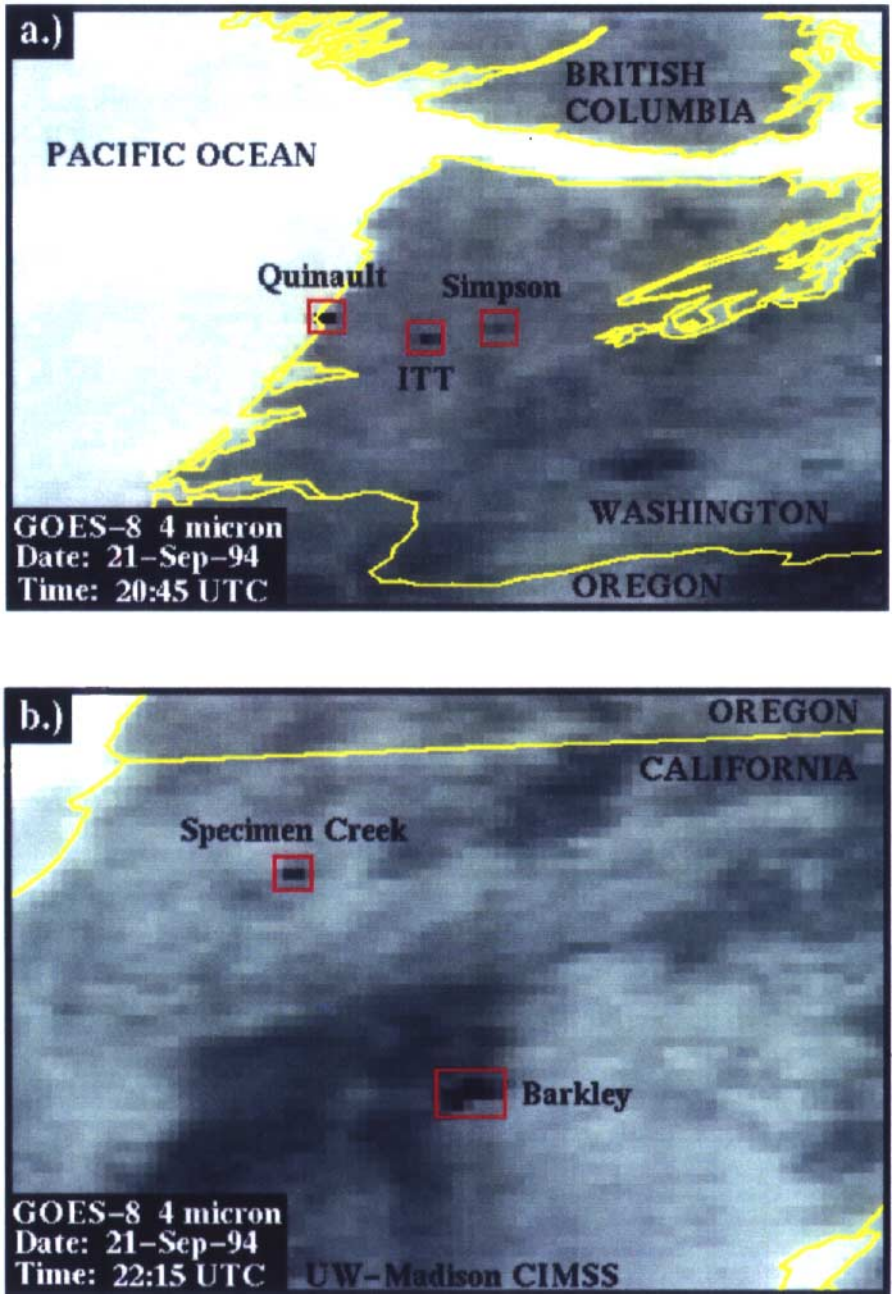

Figure 1. Fires identified in the GOES-8 4 μm imagery during the SCAR-C field experiment, including (a) the Quinault, ITT, and Simpson prescribed burns in Washington and (b) the Specimen Creek and Barkley wildfires in California. (Menzel and Prins, 1996a).

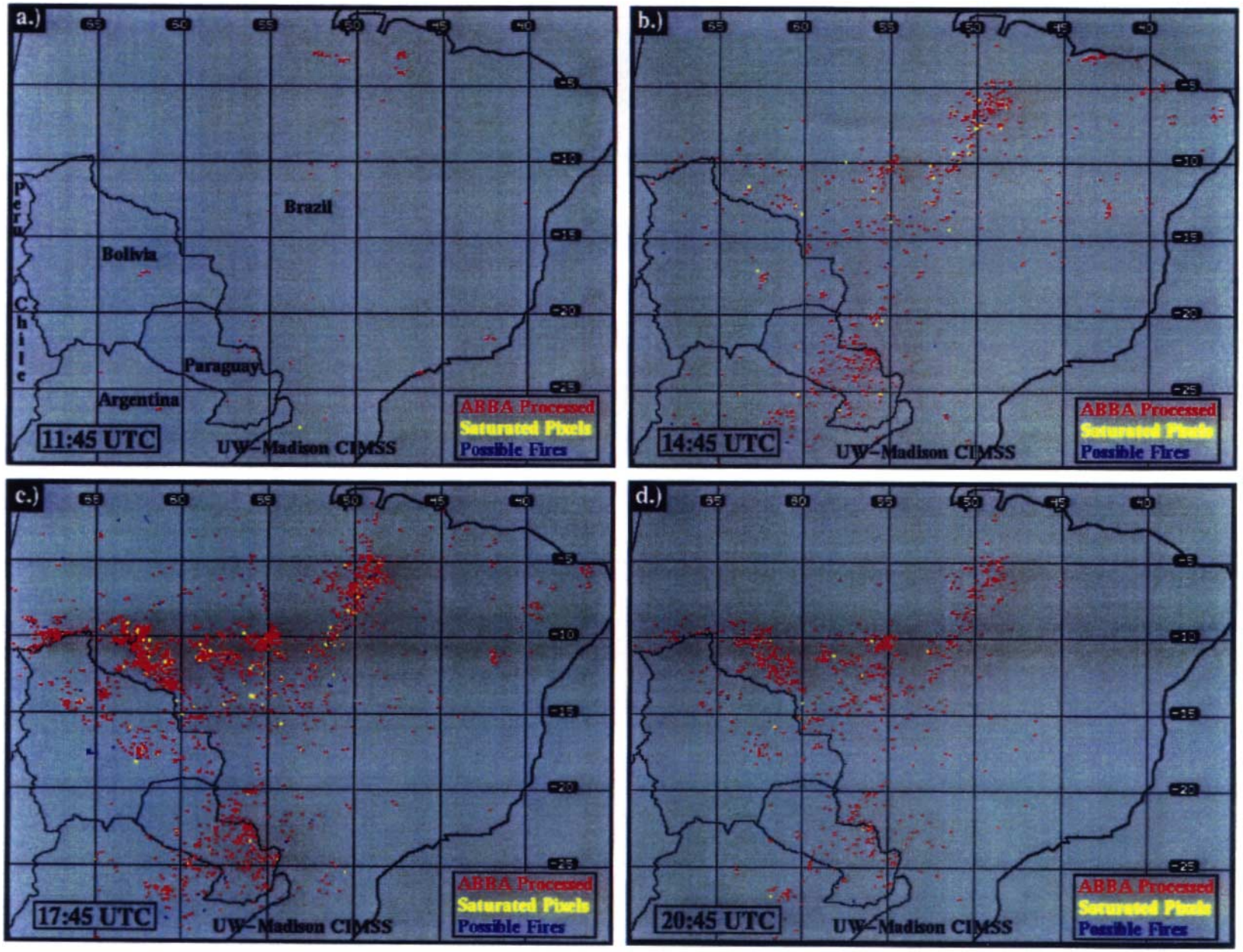

Figure 2. Fires detected by the initial GOES-8 ABBA on 24 August 1995 at (a) 1145 UTC, (b) 1445 UTC, (c) 1745 UTC and (d) 2045 UTC. Red markers indicate the locations of fire pixels processed with the GOES-8 ABBA; yellow markers indicate saturated fire pixels which could not be processed; blue markers represent possible fire pixels which were not processed due to cloud contamination. (Prins and Menzel, 1996b)

Figure 3. POES-AVHRR near infrared data (0.73 - 1.1 μm) for the Okavanga region, northwestern Botswana from August 31, 1989. The burn scar resulting from a large fire, which continued to burn for several days in early September, is clearly identified by its low reflectance in the near infrared. Pixels containing actively burning fire (superimposed in white) line the edge of the large scar.

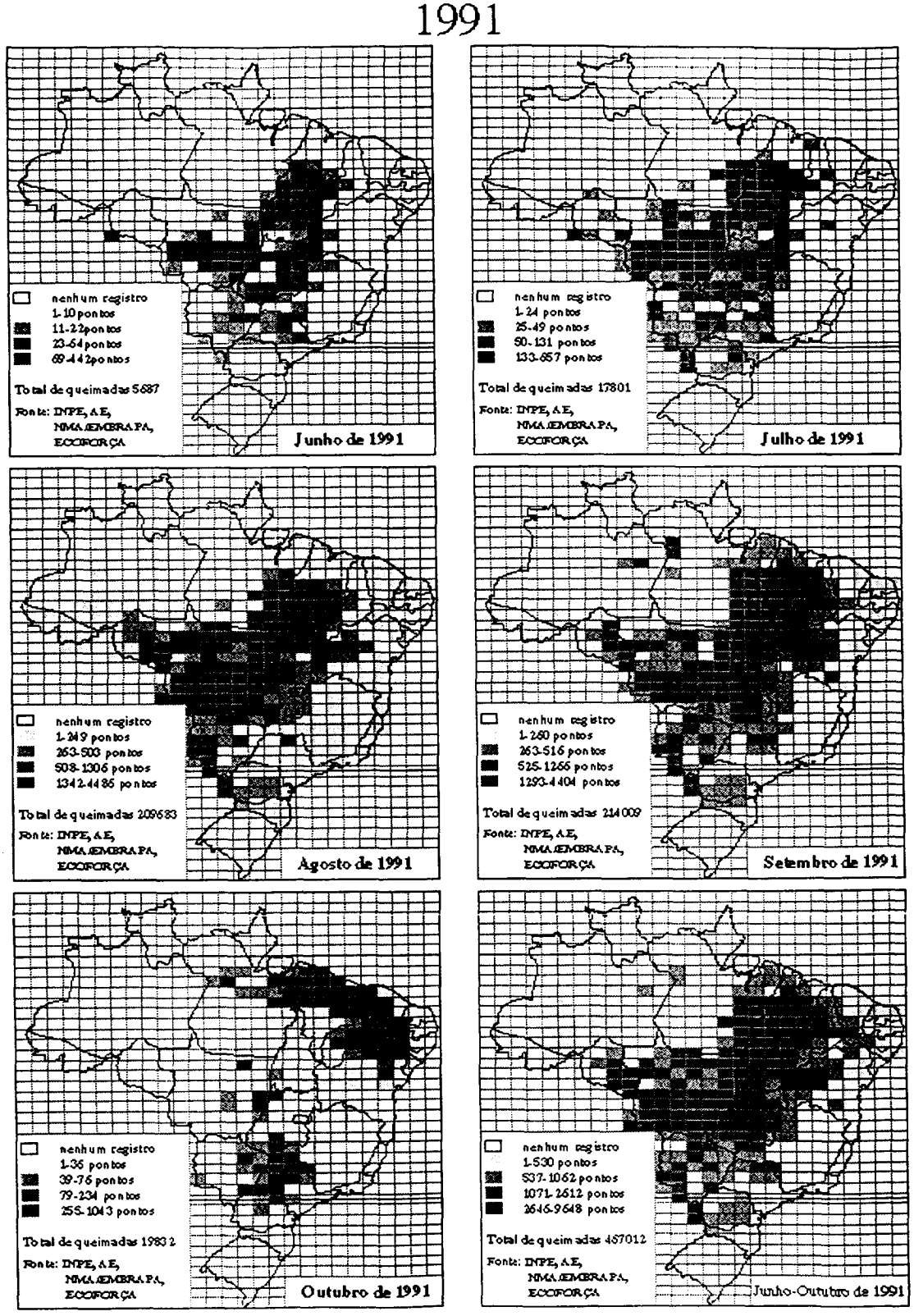

Figure 4: Sequence of maps showing the number of AVHRR fire pixels detected over Brazil in each month of the unusually dry season of 1991. Data were obtained daily from the AVHRR channel 3 images (3.55 -3.9m) of the afternoon overpasses of NOAA-11. Original data from INPE; maps produced by NMA-EMBRAPA/ECOFORCA/Ag.ESTADO, Brazil.

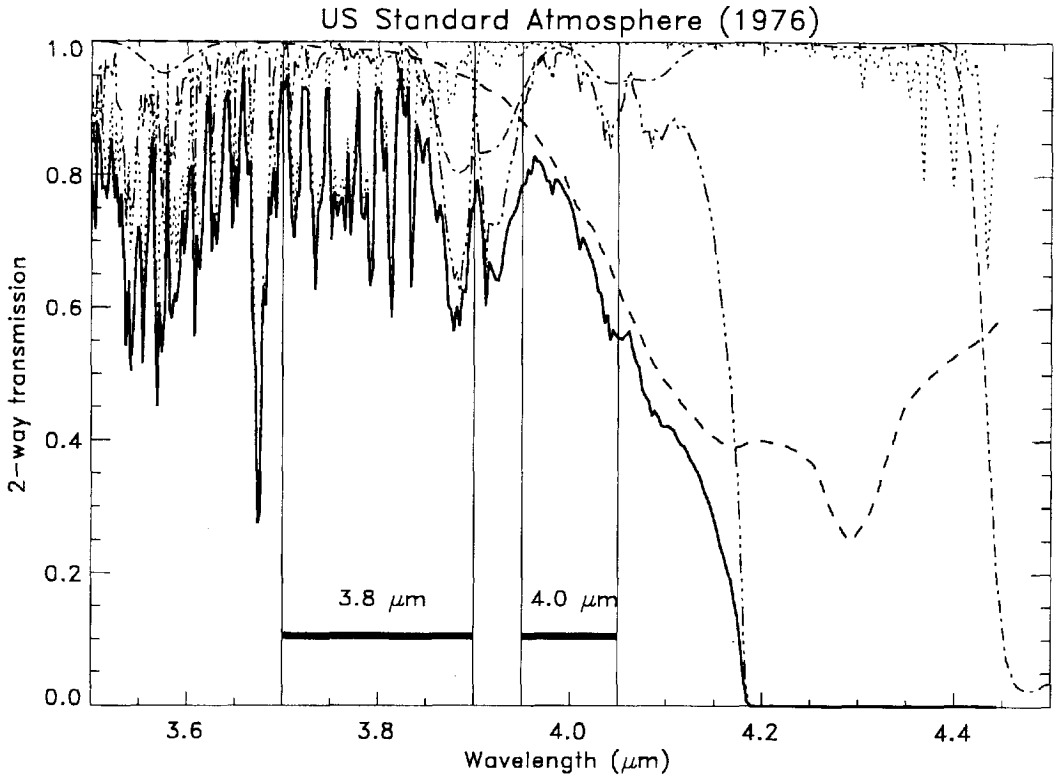

solid line = total transmission

dotted line = H2O vapor transmission

dashed line = N2 transmission

dot-dashed line = N2O transmission

dot-dot-dot-dashed line = CO2 transmission

Fig 5 Plot of the spectral two way transmission in the mid-IR (thick solid line) and the location of the two MODIS mid-IR channels (thick black bars). The contribution to the reduction in the transmission from absorption by water vapor (dotted red line), N2 (dashed black line), N2O (dot-dashedgreen line) and CO2 (dot-dot-dot-dashed blue line) are **shown.** While the absorption at 3.8 is affected mainly by water vapor aborption, the absorption at 4 μm is dominated by N2 absorption.

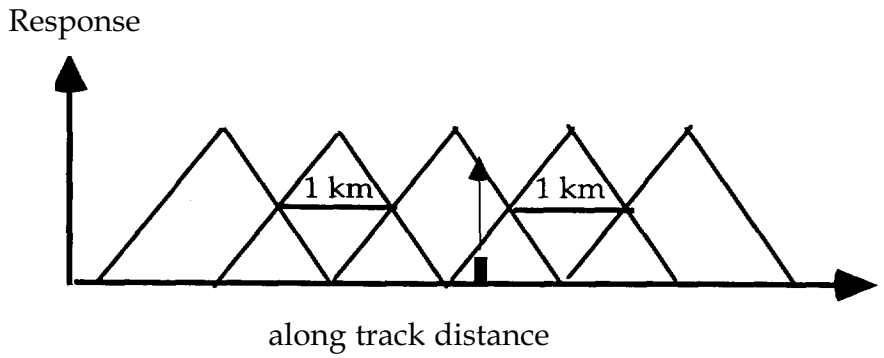

Fig.6: The MODIS response across track and the definition of the MODIS pixel. A fire in a given location (black bar in the middle of the abscissa) can be observed by two adjacent pixels as indicated by the arrow.

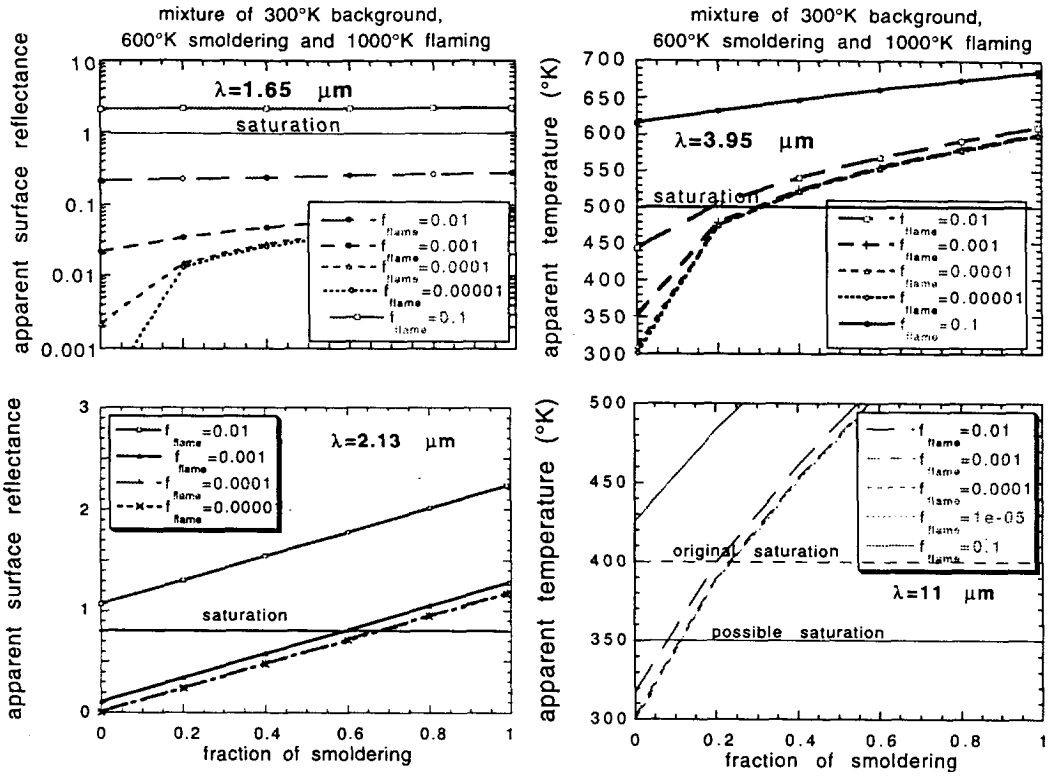

Fig. 7: The sensitivity of the MODIS channels to the fraction of the pixel covered by flames of l000K (f_{flame}), and fraction of the pixel covered by smoldering of 600K. The rest of the pixel is assumed to have a temperature of 300K.

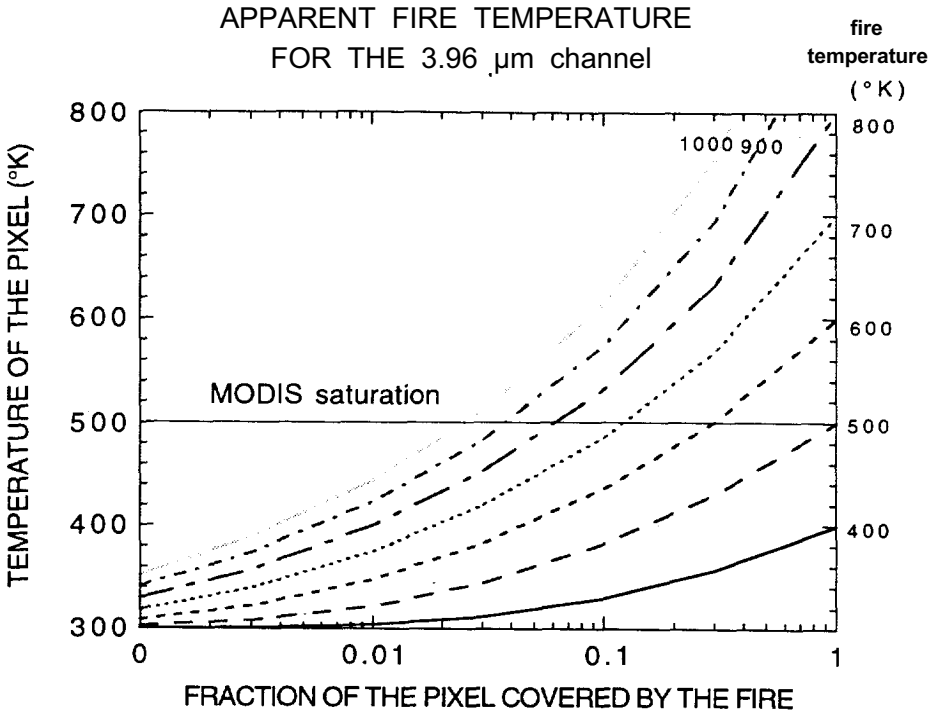

Fig. 8: The apparent temperature of the pixel at 4 μm, as observed by MODIS, as a function of the fraction of the pixel covered by the fire and its temperature.

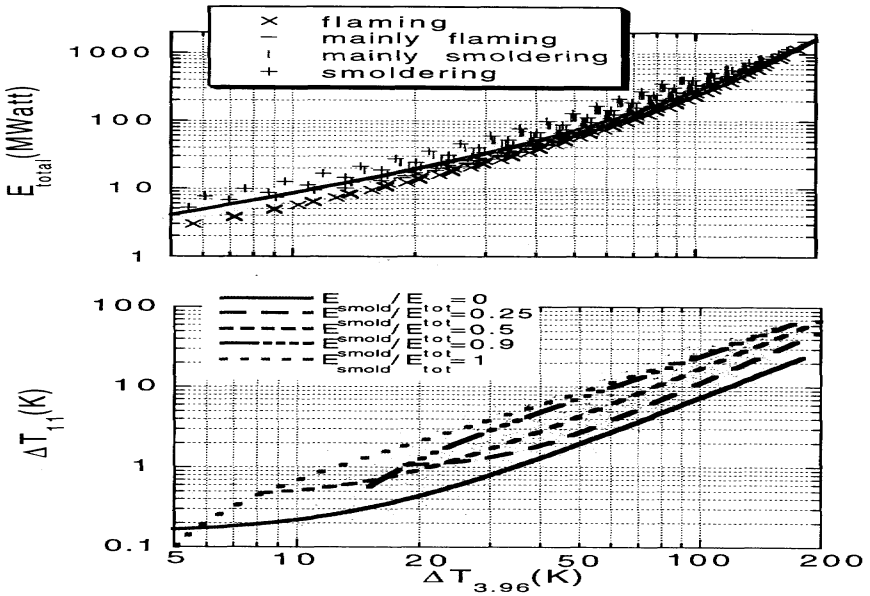

Fig. 9: Relationship between the total energy emitted from the fire Ef (E_{total}), the apparent temperature of the pixel at 11 μm and the apparent temperature at 4 μm (T4). Ef can be computed from T4 using the solid line approximation in (a) given by $Ef=4.34*10^{-19}(T4^8-T4b^8)$, where T4b is the background apparent temperature. The figure is constructed from a compilation of values for thousands of fire scenaria defined by the temperature of the smoldering phase, the temperature of the flaming phase and the fraction of the 1 km^2 pixel that is occupied by each of them. T11 is also sensitive to the ratio of smoldering/flaming and can be used to derive it.

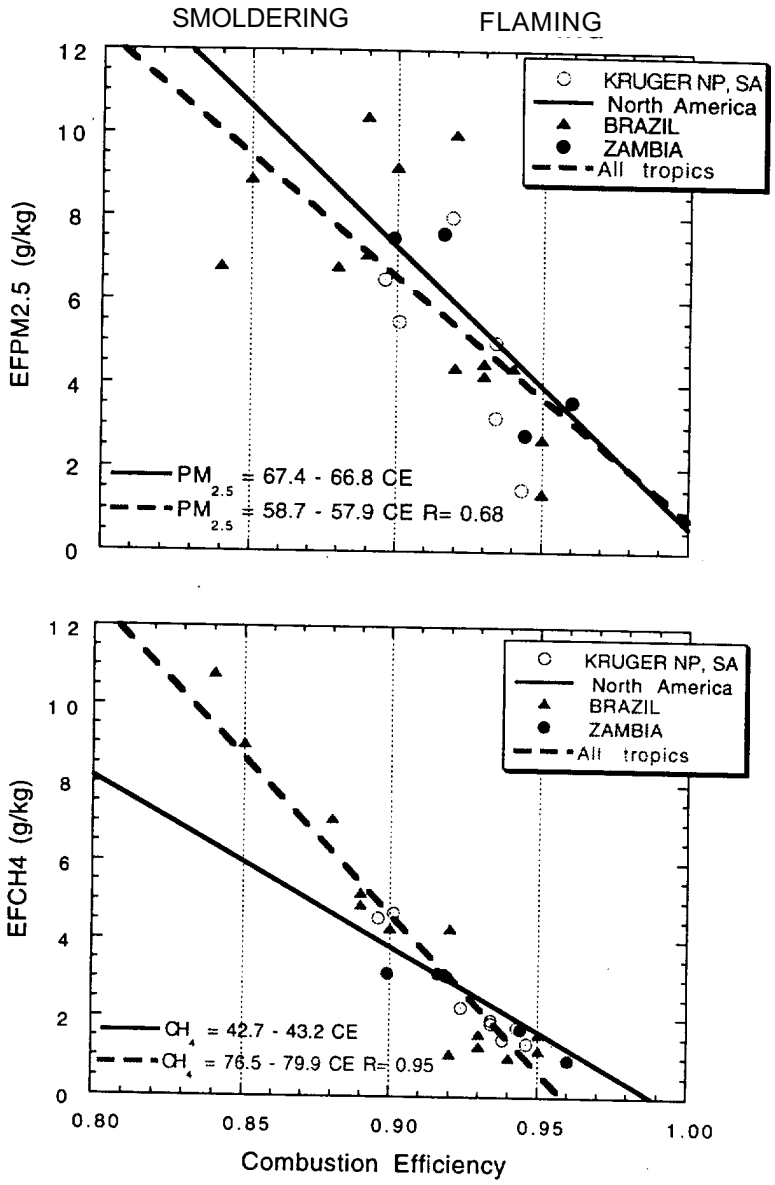

Fig 10: The sensitivity of the emission factors for particulates with size under 2.5 μm and for CH4 as a function of the modified combustion efficiency defined as the ratio of carbon emitted as CO2 to the sum of CO+CO2. The data are a compilation of measurements in the tropics (Brazil - Ward et al., 1992 nd Africa - Ward et al., 1996). For comparison the average relationship for North America determined by Ward and Hardy (1991) is also showned. Smoldering fires have combustion efficiency around 85% and flaming fires around 95% (Ward et al., 1992).

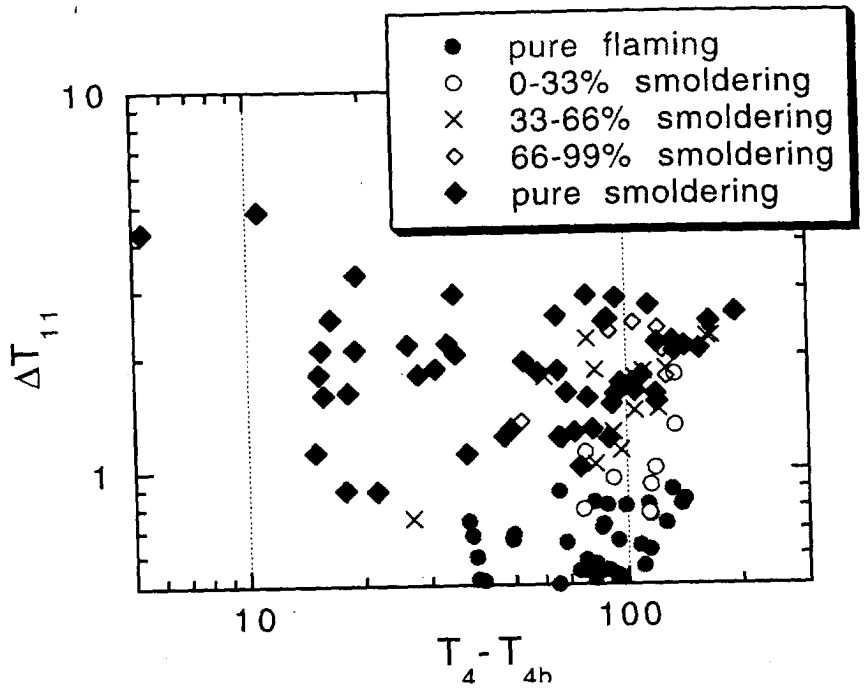

Fig. 11: Residue signal at 11 μm that is used to differentiate between smoldering and flaming: sTll =dT11 /(0.0057dT4$^{1.1}$), plotted as a function of the fire signal at 4 μm, dT4. The thresholds of sT11 that separate between smoldering and flaming are:

If sT11 <1.0K	then flaming stage
If sT11 > 1.7K	then smoldering stage
Otherwise:	a mixed stage

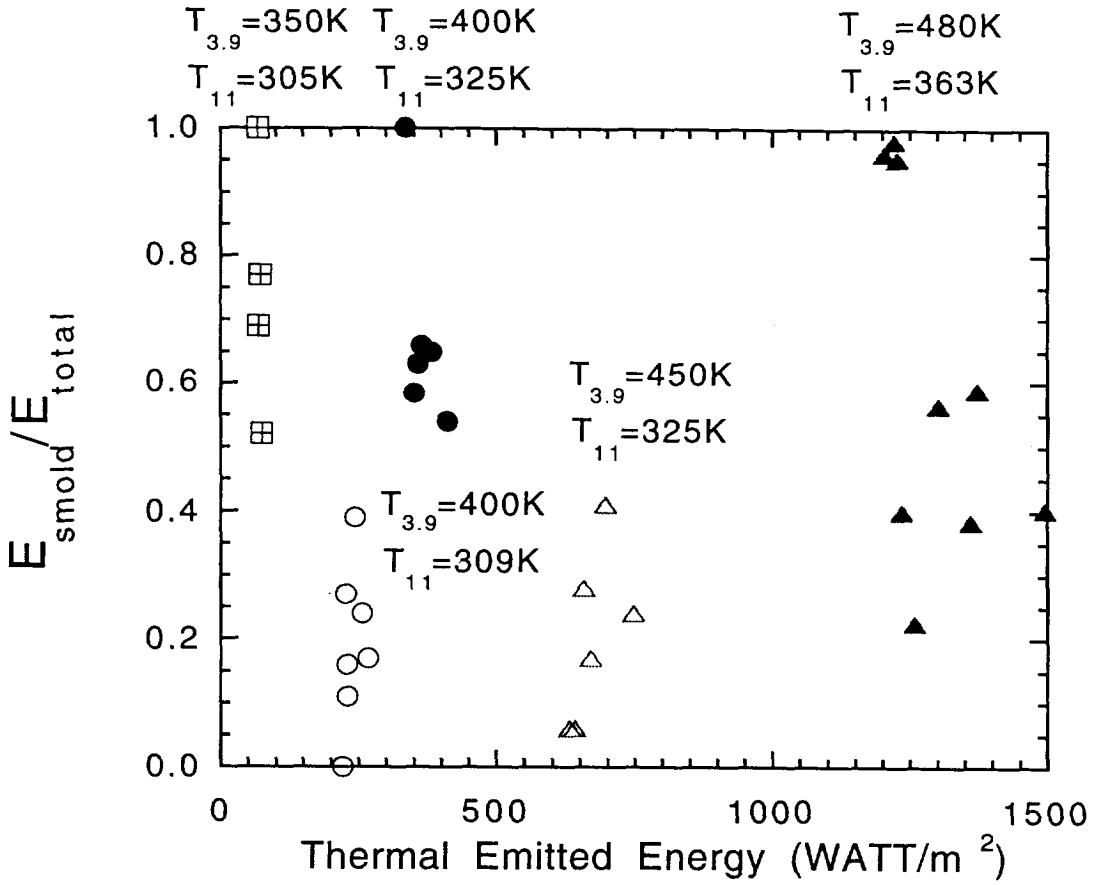

Fig. 12: Simulation of different combinations of fire temperatures and sizes in the flaming (1000K±200K) and smoldering (600K±l00K) stages that give the same response in the MODIS 4 and 11 μm channels. Each symbol is a set of examples of combinations of fire energy and smoldering to total ratio that corresponds to the apparent temperatures given on the top of the set.

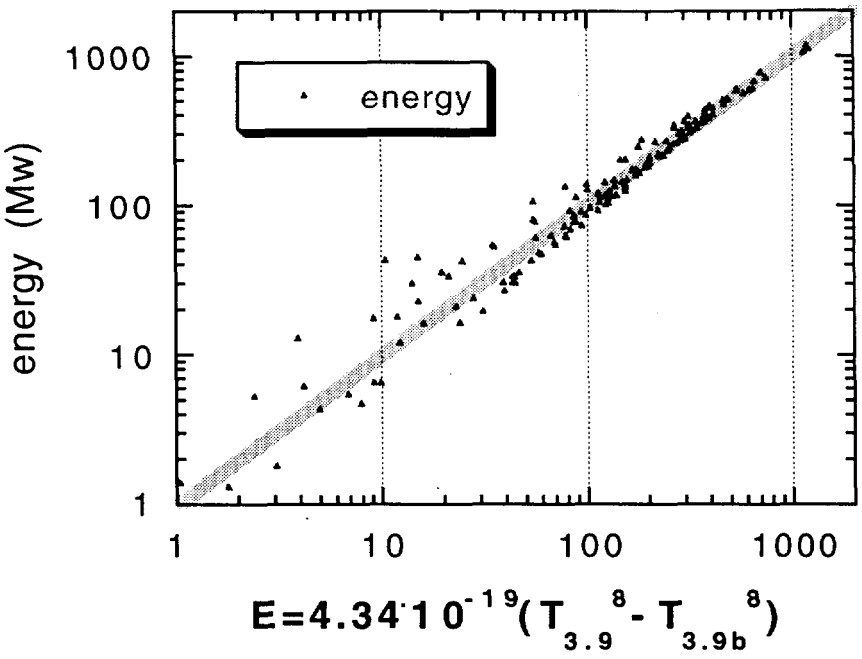

Fig. 13: Simulation of the effect of fire heterogeneity on the retrieval of fire thermal energy. A comparison is plotted between the simulated and retrieved fire energy. 150 fire pixels were simulated. Each composed of 500 zones with different temperature but following Gausian distributions around an average background, smoldering and flaming temperatures. The fraction of smoldering and flaming varies from pixel to pixel. The average temperatures and standard deviations vary too. The simulated fire energy is the sum of the energies in the 500 zones. The retrieved fire energy is retrieved from the average radiance at 4 μm. It fits the simulated energy very well. The average standard deviation in deriving the fire energy is 16%. It is larger for small fires and smaller for energetic fires.

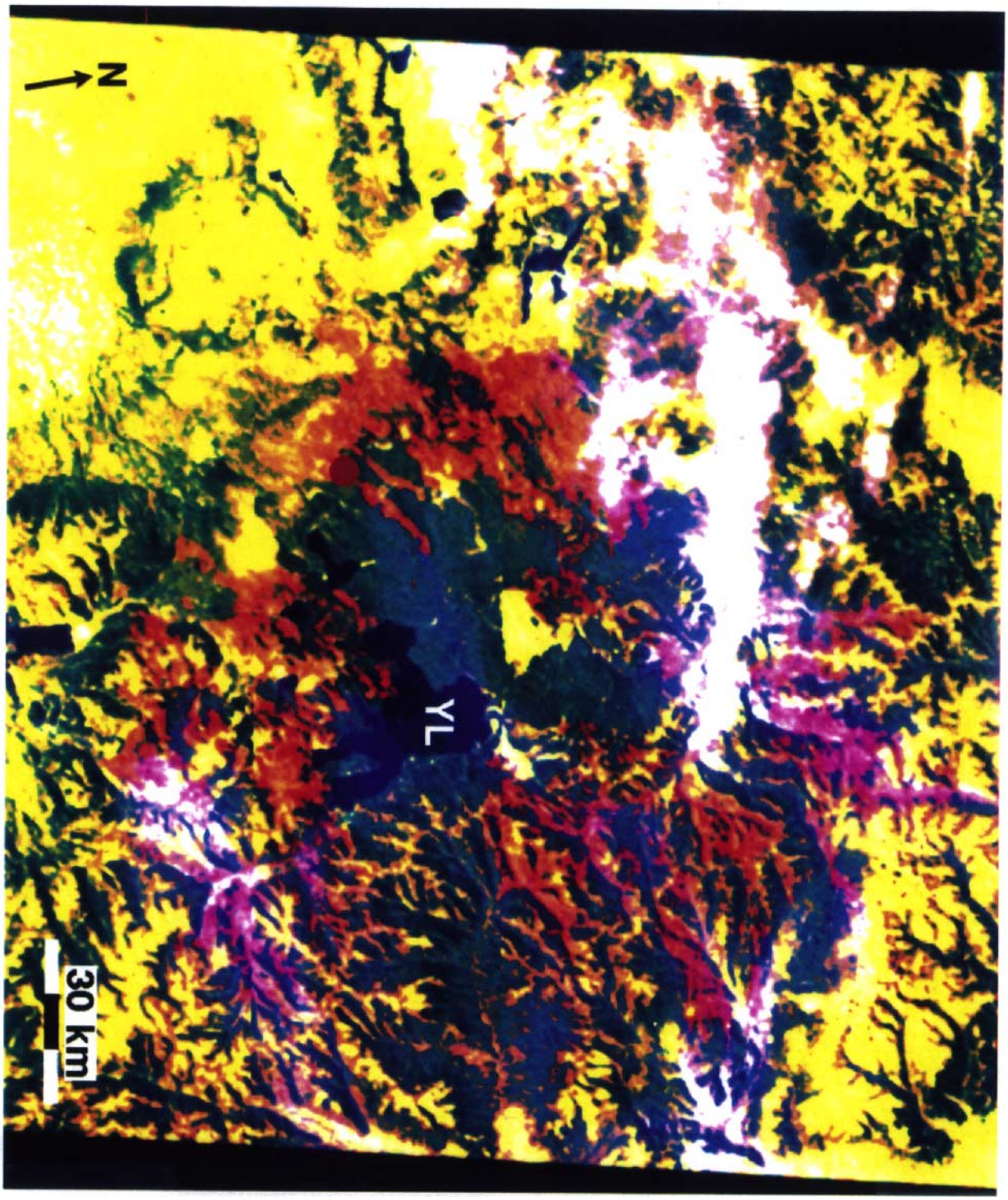

Fig. 14: Image of 210 km x 180 km of the Yellowstone National Park fire area at 500 m/pixel spatial resolution. The image is a false color composite generated using TM data at 2.2 µm, 1.65µm, and 0.66 µm, which were resampled to create MODIS corresponding channels 7, 6, and 1. A distance scale marking 30 km is located in the lower right part of the image, while a north arrow indicator is in the lower left. In this false color scheme the unburned forest is deep green, large water bodies (for example, Yellowstone Lake denoted by "YL" in the image) are dark blue, and clouds are white. Active fires are bright pink, while recent burn scars (< 3 days old) are brick red. Older burn scars are included in the yellow portions of the image. As a reference point, Old Faithful Visitor Centcr is indicated with a bright red dot towards the center of the image.

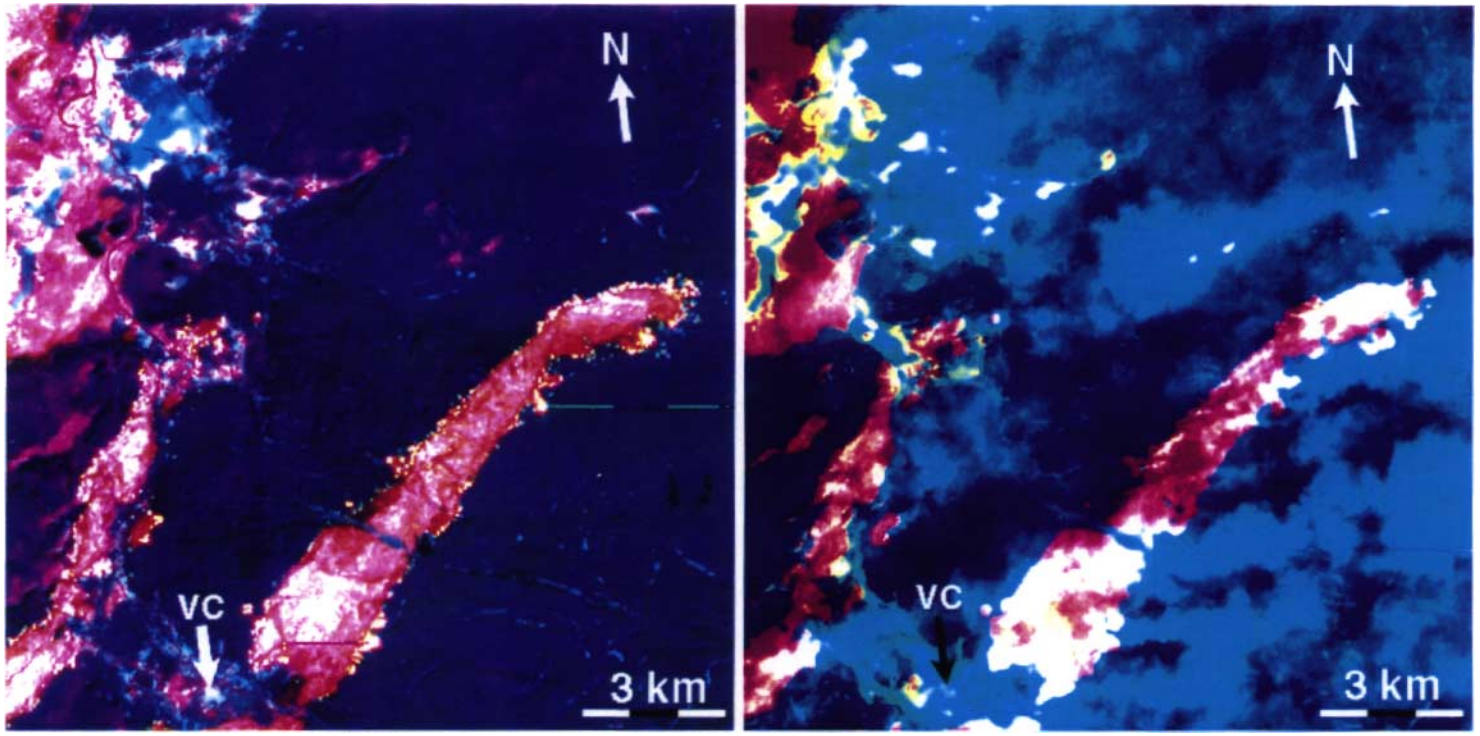

Fig. 15: A 15 km x 15 km subarea of Fig. 13 at 30 m/pixel spatial resolution. A firestorm passed over the Old Faithful Visitor Center (marked VC) 19 hours before the data were acquired. (a) is a false color of 11 μm (red), 2.2 μm (green), and 1.65 μm (blue) combination which shows the recent burn scars in pink and red, and active fires in yellow-white. (b) is a false color of 11 μm (red), 0.66 μm (green), 0.48 μm (blue) combination which shows the outline of the burn scars (red and white) along with the associated smoke plumes (blue) generated from especially strong fires. White areas have high radiances in all bands which means that they are smoke-covered active fires, burn scars, or natural thermal springs.

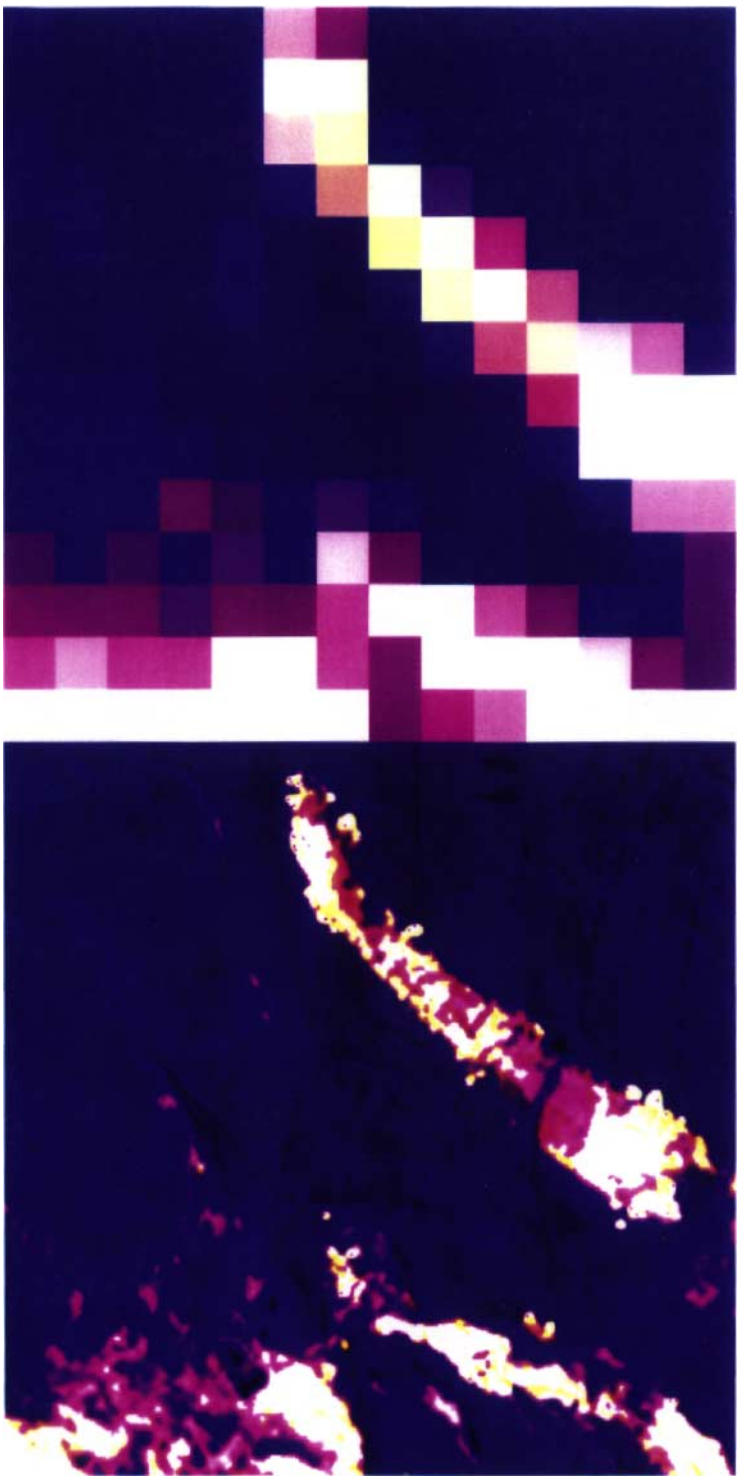

Fig. 16: Images of the same area as in Fig. 14, but here the TM data were resampled and rescaled to simulate MODIS channels at 11 μm, 4 μm, and 1.65 μm, which in the image are red, green, and blue, respectively. (a) - 30 m/pixel spatial resolution data, (b) - resampled to the MODIS 1 km data. The white/yellow areas represent relatively high concentrations of active fires (high radiances in all bands), while the reddish-pink areas are either burn scars or natural thermal springs and mud pots. The two primary fire areas shown in this image advanced from the lower left corner of the image (SW) towards the upper right corner of the image (NE).

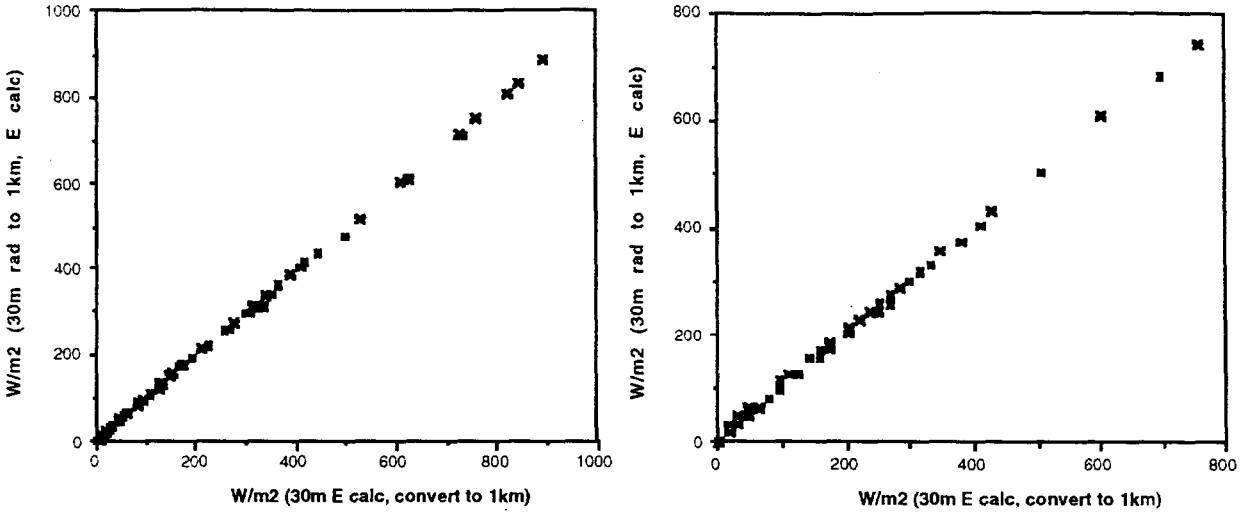

Fig. 17: Comparison of the energy calculated in two ways from a single data set, corresponding to Fig. 15. The first method (x-axis) is to calculate the energy of each 30 m pixel and then resampled to lkm/pixel spatial resolution, while the second method (y-axis) is to calculate the energy by resampling the 30 m radiances to 1 km spatial resolution, and then converting to energy. (a) - results for a straight average resulting in 196 (14 x 14) rectangular pixels, (b) - results for the MODIS triangular conversion. Clusters of points near 500 W/m^2 represent the pixels radiating at background temperatures (303 K). Contrary to intuition, the produced curve does not exactly match a line having a slope of 45°. Rather it is slightly bowed upwards, showing that for identical fire areas, averaging radiances to 1 km first and then calculating energies (i.e., the MODIS instrument) will result in higher energy values than those obtained from higher spatial resolution data.

Fig 18: Observations of fire and smoke from the MAS imagery for the Quinault fire for the first pass of the ER-2 above the fire. On the right is a MAS false color image showing the shore line and the fire and smoke at 19:12 GMT. The fire zone is expanded into the image in the left top and the calculations of the thermal energy emitted from the fire is shown in the bottom left.

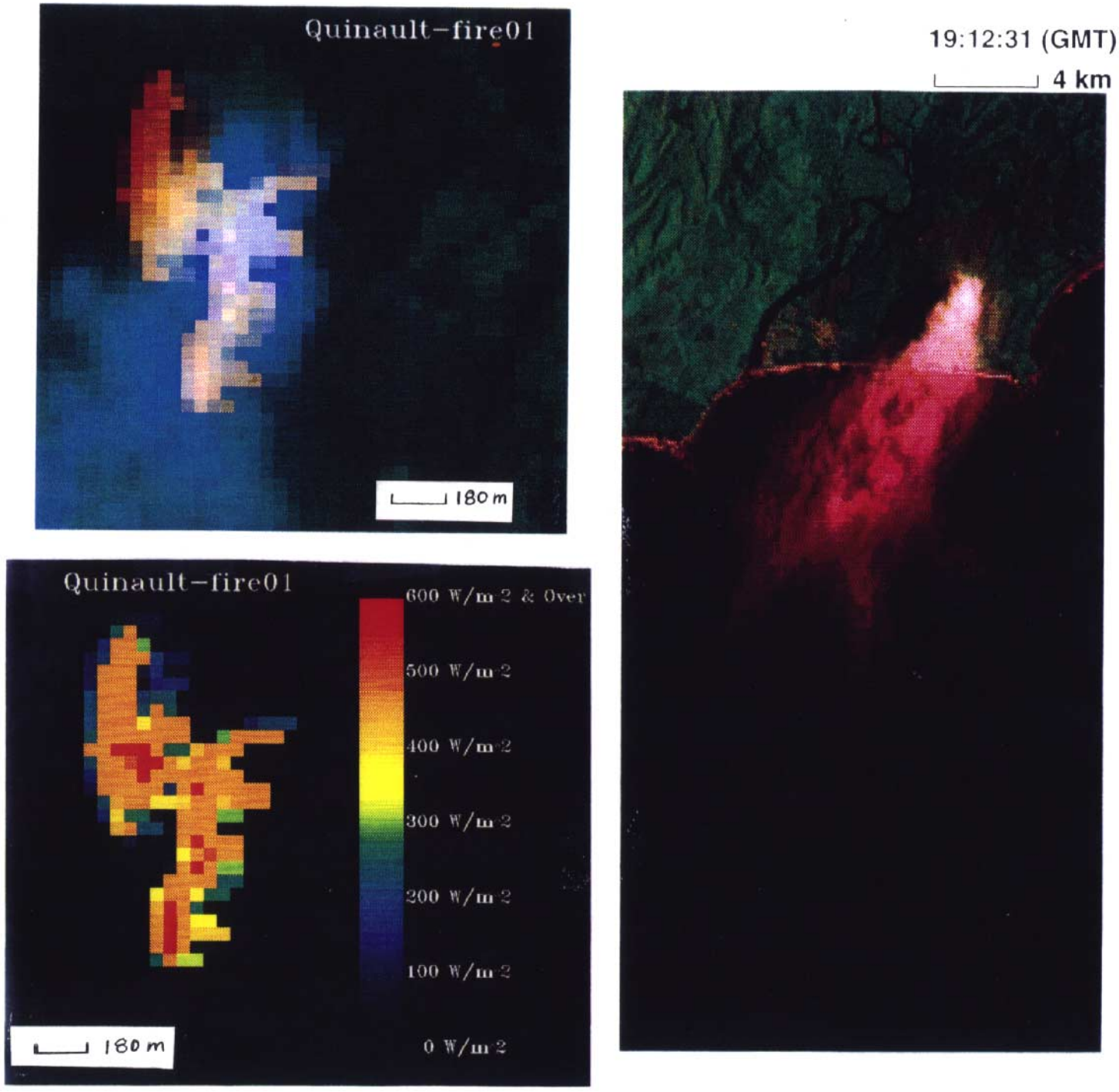

Fig 18: Observations of fire and smoke from the MAS imagery for the Quinault fire for the first pass of the ER-2 above the fire. On the right is a MAS false color image showing the shore line and the fire and smoke at 19:12 GMT. The fire zone is expanded into the image in the left top and the calculations of the thermal energy emitted from the fire is shown in the bottom left.

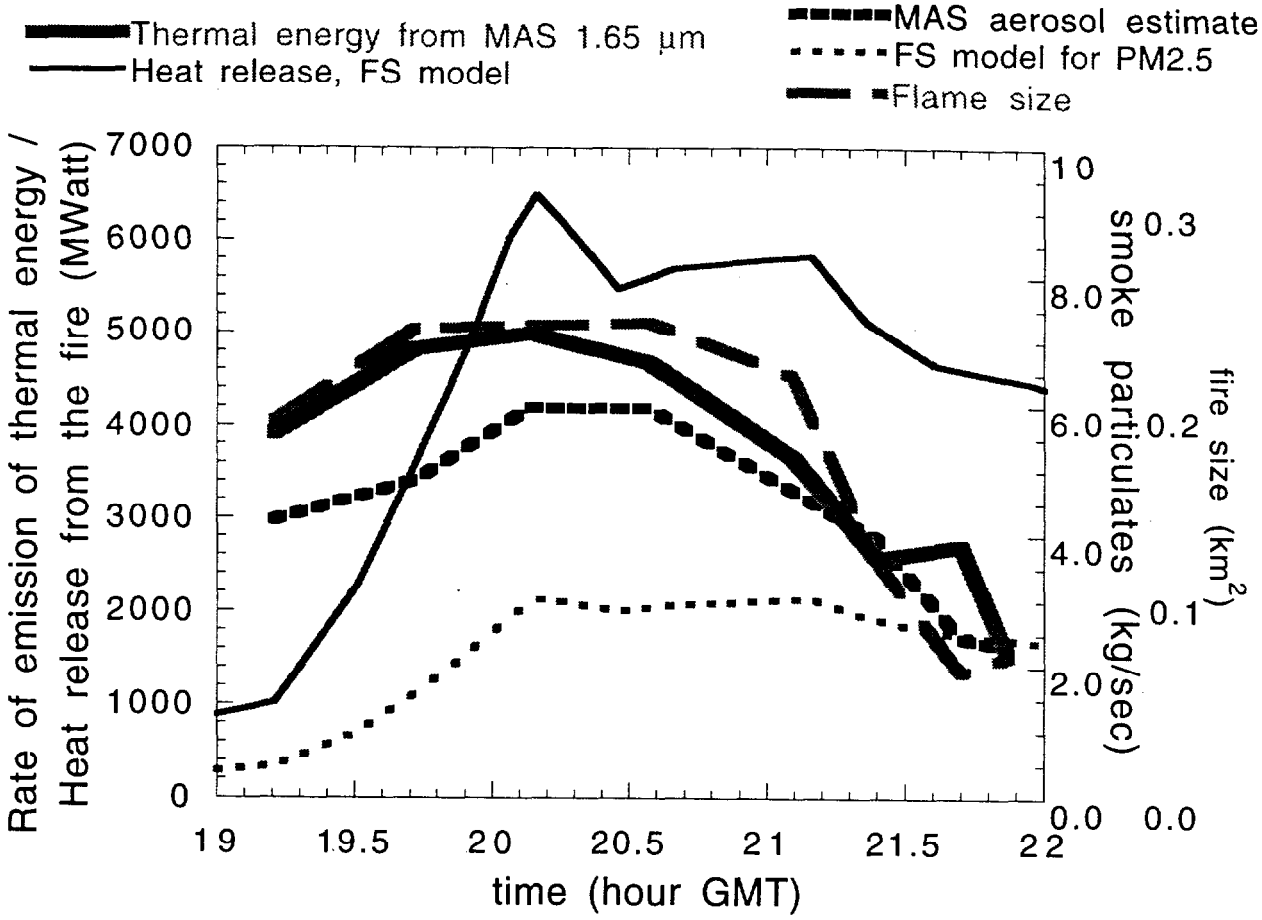

Fig. 19: Relationship between the rate of emission of thermal radiative energy from the Quinault fire and the rate of emission of smoke particulates from the fire. The thermal radiation is computed from MAS observations at 1.6 μm assuming that each pixel is a black body. The rate of emission of smoke particulates is derived from MAS observations of the smoke over the water downwind from the fire at 0.66 μm. The results are compared with the size of the fire detected by MAS at 4 μm and the model predictions of the Forest Service for the heat release and for the total particulate mass for size under 2.5 μm. The model is based on ground based observations of the fuel load, ignition and consumption. Note the strong similarity between the time dependence of the rate of emission of radiative energy, the fire size and the rate of emission of smoke as obtained from the remote sensing data.

Figure 20. High temperature sources detected in l-kilometer POES-AVHRR infrared data from June 25, 1992. Global AVHRR coverage provided by the IGBP-DIS global l-km data set courtesy of USGS Eros Data Center.